



Eidgenössische Technische Hochschule Zürich
Swiss Federal Institute of Technology Zurich



Master of Science Thesis
November 2018

Asymmetric Diffusion Encoding for High-Resolution Diffusion Tensor Imaging

Alen Mujkanović

Supervisors:

Dr. Christopher Nguyen, Harvard Medical School and MGH

Prof. David Sosnovik, Harvard Medical School and MGH

Prof. Sebastian Kozerke, ETH Zürich

Department of Electrical Engineering and Information Technology
Swiss Federal Institute of Technology (ETH Zürich), Zurich, Switzerland

Abstract

Magnetic Resonance Diffusion Tensor Imaging (MR-DTI) allows *in vivo* fiber tracking and is primarily used to study brain connectivity. Due to the long encoding procedure required to measure the small self-diffusion of water in tissues the method is particularly susceptible to low signal-to-noise ratios and motion artifacts (1). This makes cardiac and abdominal applications challenging. Short diffusion encoding also enables longer readout durations, permitting high-resolution acquisitions. Asymmetric encoding schemes can be utilized to achieve equivalent diffusion-weighted encoding as traditional symmetric pulse encoding. Signal deterioration and distortion due to secondary gradient effects (concomitant fields / eddy currents) are generally not compensated for asymmetric waveforms (2). In the present work, a method was devised to find optimal encoding sequences eliminating concomitant gradient (CG) perturbations using a convex optimization framework. The generated Concomitant-Compensated (COCO) waveforms were evaluated against symmetric and modified Convex Optimized Diffusion Encoding (CODE) gradient waveforms (3) in imaging experiments at gradient amplitudes up to 270 mT/m.

The optimized waveforms show a reduction in echo time (TE) for all asymmetric diffusion encoding gradient (DEG) waveforms. The magnitude of the reduction compared to equivalent symmetric waveforms was up to 33% for CODE and 17% for COCO. Simulations of the diffusion encoding show the magnitude of CG effects for non-compensated waveforms and an absence of attenuation for all COCO waveforms. Increased uniformity of apparent diffusion coefficient (ADC) maps is achieved compared to the non-compensated asymmetric waveforms and was shown in water phantom acquisitions. An *in vivo* brain diffusion-weighted imaging experiment was carried out, showing reduced ADC bias caused by CG attenuation. The motion-robustness was verified with a cardiac diffusion tensor imaging (DTI) experiment carried out *in vivo*. For a large field of view (more than ~20 cm) or high gradient amplitudes (above 80 mT/m), CG effects are substantial and compensation indispensable. The implemented COCO waveforms fully eliminate CG fields in simulation and show significant reduction of gradient-related artifacts in image acquisition, while reducing TE. This enables motion-robust high-resolution DTI for investigation of future clinical applications.

Acknowledgements

Our contributions are never a single-handed effort. Here I devote a small space to acknowledge all the people that have supported me throughout my thesis and made my stay in Boston a transformative experience that has opened me to previously unimagined possibilities.

First and foremost, I would like to thank my supervisors for the confidence they had in my ability to complete this project and providing me with this opportunity. Thanks to Sebastian Kozerke for his guidance and patience and to David Sosnovik for helping me feel welcomed and establishing contacts at the Cardiovascular Research Center and Martinos Center. A special thanks to Chris Nguyen for his commitment and constant support. A thanks also to colleagues at Martinos, CVRC and BWH for their technical support and insights, to Filip Szczepankiewicz, Susie Huang, Thomas Witzel, Anastasia Yendiki, Maaike van den Boomen, Mohammed Mahamdeh and the people at the Quantitative Tumor Imaging Lab (QTIM). Thanks also to Bruce Rosen for cultivating the spirit in the Martinos Center student community. Further, I would like to thank all the wonderful people who brightened my days in Boston and making it such a delightful time. My deepest gratitude goes to my family for the never-ending support without which I would not have the courage to pursue my dreams. A special mention goes to Putumayo World Music for setting the tune to the many hours of work invested in this project.

Finally, I would like to express my gratitude to the Josef P. und Nelly Spiess-Mohn Foundation, the Vontobel Foundation and the ETH Financial Aid Office for financially assisting my academic pursuits.

"Scientific endeavours with their positive and negative aspects are an integral part of humanity. We are forced to live with them whether we want or not and try to make the best out of it. But, we have also to accept the concerns of those who rather see the threatening aspects of science, that merely put into evidence the threatening side of the human nature."

*- Richard R. Ernst (*1933), Nobel Prize Acceptance Speech 1991*

Contents

1	Introduction.....	1
1.1	Imaging Molecular Diffusion.....	1
1.2	Challenges in Diffusion MRI.....	2
1.3	Gradient Waveform Optimization.....	4
2	Theory.....	5
2.1	Diffusion MRI Basics.....	5
2.1.1	Physics of Molecular Diffusion.....	5
2.1.2	Magnetization Evolution.....	7
2.1.3	Diffusion Encoding Gradient Waveforms.....	7
2.2	Diffusion Metrics and Visualization.....	10
2.2.1	Diffusion-Weighted Imaging (DWI)	10
2.2.2	Diffusion Tensor Imaging (DTI)	11
2.3	Gradient Effects.....	14
2.3.1	Gradient Moments.....	14
2.3.2	Eddy Currents.....	15
2.3.3	Concomitant Gradient Fields	16
2.4	Convex Optimization.....	17
3	Methods.....	19
3.1	Gradient Waveform Optimization.....	19
3.1.1	Problem.....	19
3.1.2	Constraints.....	21
3.1.3	Concomitant Gradient Compensation.....	21
3.1.4	Waveform Simulation.....	22
3.2	Imaging Experiments.....	23
3.2.1	Phantom Imaging.....	23
3.2.2	<i>In Vivo</i> Brain Imaging.....	24
3.2.3	<i>In Vivo</i> Heart Imaging	24
3.3	Error and Noise Quantification.....	26

4	Results and Evaluation.....	27
4.1	Waveform Simulation	27
4.1.1	Echo Time Reduction.....	27
4.1.2	Concomitant Gradient Compensation.....	29
4.1.3	Gradient Moment Evolution.....	32
4.2	Evaluation of Imaging Experiments	33
4.2.1	Phantom Acquisitions.....	33
4.2.2	<i>In Vivo</i> Brain DWI.....	35
4.2.3	<i>In Vivo</i> Cardiac DTI.....	37
5	Conclusion.....	39
	Appendix.....	41
	Bibliography.....	43

List of Figures

Figure 1.1: Ambiguity of crossing fibers within a single voxel	3
Figure 2.1: Evolution of probability distributions in one dimension	6
Figure 2.2: MRI phase evolution of diffusing vs. stationary spins.....	8
Figure 2.3: Stejskal-Tanner pulse sequence diagram	9
Figure 2.4: Depiction of DWI spin echo pulse sequence.....	10
Figure 2.5: Diffusion tensor visualization	12
Figure 2.6: Symmetric diffusion encoding sequences	15
Figure 3.1: Waveform optimization process flowchart.....	20
Figure 3.2: Comparison of optimized waveforms.....	23
Figure 3.3: Illustration of cardiac helix angle.....	25
Figure 4.1: Minimum echo time achieved for a range of b -values	27
Figure 4.2: Comparison of echo time reduction	28
Figure 4.3: Concomitant gradient phase accumulation during encoding	29
Figure 4.4: Simulation of concomitant field attenuation in a simulated imaging volume	30
Figure 4.5: Effect of resolution on concomitant fields.....	31
Figure 4.6: Evolution of gradient moments during diffusion encoding	32
Figure 4.7: ADC maps from phantom experiments.....	33
Figure 4.8: ADC maps from phantom experiments at high gradient amplitudes.....	34
Figure 4.9: <i>In vivo</i> brain ADC maps.....	35
Figure 4.10: <i>In vivo</i> brain ADC maps acquired at $G_{max} = 150 \text{ mT/m}$ and $b = 500 \text{ s/mm}^2$	36
Figure 4.11: Visualization of <i>in vivo</i> heart helix angle and absolute errors	37

List of Tables

Table 2.1: Typical ADC values of biological tissues and water	10
Table 3.1: Overview of constraints for the proposed optimization problem.....	21
Table 3.2: Overview of concomitant attenuation simulation parameters	22
Table 3.3: <i>In vivo</i> brain imaging parameter combinations.....	24
Table 4.1: TE reduction of asymmetric relative to symmetric waveforms	28

Nomenclature

In this section you can find a non-exhaustive list of acronyms and abbreviations in alphabetical order, mathematical operators, and physical quantities given roughly in order of appearance.

Acronyms and Abbreviations

ADC	Apparent Diffusion Coefficient
AF	Attenuation Factor
AUTOSEQ	Automated Pulse Sequence Generation
CG	Concomitant Gradients
CMR	Cardiovascular Magnetic Resonance
CNR	Contrast-to-Noise Ratio
COCO	Concomitant Compensated (DEG Waveform)
CODE	Convex Optimized Diffusion Encoding
COV	Coefficient of Variation
DEG	Diffusion Encoding Gradient
DTI	Diffusion Tensor Imaging
DWI	Diffusion-Weighted Imaging
EC	Eddy Currents
ECG	Electrocardiography
EN-CODE	Eddy Current-Nulled Convex Optimized Diffusion Encoding
EPI	Echoplanar Imaging
FA	Fractional Anisotropy
FOV	Field of View
GRAPPA	Generalized Auto-calibrating Partial Parallel Acquisition
HA	Helix Angle
HCP	Human Connectome Project
IVIM	Intravoxel Incoherent Motion
MD	Mean Diffusivity

MOCO	Motion Corrected (DEG Waveform)
MODE	
MONO	Monopolar (DEG Waveform)
MR	Magnetic Resonance
MRA	Magnetic Resonance Angiography
MRE	Magnetic Resonance Elastography
MRI	Magnetic Resonance Imaging
NMR	Nuclear Magnetic Resonance
ODGD	Optimized Diffusion-weighting Gradient waveform Design
px	Pixel
RA	Relative Anisotropy
RF	Radiofrequency
RMSE	Root Mean Square Error
ROI	Region of Interest
SDP	Semidefinite Programming
SE	Spin Echo
SENSE	Sensitivity Encoding
SNR	Signal-to-Noise Ration
TE	Echo Time
VR	Volume Ratio

Operators

$\square \cdot \square$	Inner product
$\square \times \square$	Cross product
$\square \otimes \square$	Outer product
$\bar{\square}$	Arithmetic mean of values
$\dot{\square}, \ddot{\square}, \dddot{\square}$	First, second and third partial derivative in respect to time
$\nabla \square$	Gradient
$\nabla \cdot \square$	Divergence
$\nabla \times \square$	Curl
$\nabla^2 \square$	Laplace operator
\square^T	Matrix transpose
$\text{sgn}(\square)$	Sign function
$\ \square\ _2$	Euclidian vector norm
$\ \square\ _*$	Frobenius or nuclear matrix norm
$\arg \max_{\square} \square$	Arguments of the maxima

Physical Quantities

Throughout the work, all vectors and tensors are depicted using a **bold** font. The same quantity written in regular font is the vector length in Euclidian norm, e.g. $r = \|\mathbf{r}\|_2$.

\mathbf{J}	Diffusion flux	[mol/s m ²]
c	Molar concentration	[mol/m ³]
D / \mathbf{D}	Diffusion coefficient / tensor	[m ² /s]
\mathbf{r}	Position in space	[m]
P	Diffusion probability density propagator	[–]
σ / σ^2	Standard deviation / Variance	[–]
$\bar{\Delta r}^2$	Mean square diffusion length	[m]
Δt	Diffusion time	[s]
\mathbf{M}	Current net magnetization	[A/m]
M_0	Net magnetization prior to excitation	[A/m]
M_{xy} / M_z	Transversal / longitudinal magnetization components	[A/m]
\mathbf{B}	Magnetic field strength	[T]
B_0	Main static magnetic field strength	[T]
γ	Gyromagnetic ratio	[Hz/T]
S	Complex-valued MR signal	[–]
b / \mathbf{b}	Diffusion sensitivity factor / matrix	[s/m ²]
\mathbf{G}	Magnetic field gradient strength	[T/m]
ϕ	Magnetization phase	[rad]
\mathbf{k}	k -space trajectory	[1/m]
Λ	Diffusion tensor eigenmatrix	[m ² /s]
$\bar{\lambda}$	Mean diffusivity	[m ² /s]
$\lambda_1, \lambda_2, \lambda_3$	Diffusion tensor eigenvalues	[m ² /s]
$\mathbf{v}_1, \mathbf{v}_2, \mathbf{v}_3$	Diffusion tensor eigenvectors	[–]
c_l, c_p, c_s, c_a	Diffusion ellipsoid linearity, planarity, sphericity, anisotropy	[–]
M_0, M_1, M_2	Gradient moments of order $i = 0, 1, 2$	[rad/m ⁱ]
B_c	Concomitant magnetic field distribution strength	[T]
ϕ_c	Residual phase due to concomitant fields	[rad]
d_{slice}	Thickness of excited image slice	[m]
Δk	k -space line spacing	[1/m]
τ	Echo spacing of EPI readout	[s]
m	Maxwell index	[T ² /m ²]
$\Delta x, \Delta y, \Delta z$	Resolution in the x, y , and z directions	[m]
d_z	Offset from isocenter along direction of bore axis	[m]

1 Introduction

1.1 Imaging Molecular Diffusion

Molecular diffusion is one of the basic types of physical transport phenomena. It plays a crucial role in all life-sustaining processes, such as respiration, absorption, circulation and excretion of metabolic products. As diffusion is directed by physical structures in the body, assessing it can be a way of inferring anatomical structure. Magnetic resonance imaging (MRI) provides a non-invasive method to assess molecular self-diffusion of water in biological tissues.

Using a sequence of magnetic gradient field and radiofrequency (RF) pulses, a diffusion-dependent contrast is generated through loss of phase coherence of diffusing versus stationary nuclei, causing an attenuation of signal magnitude in areas with higher diffusivity. Several other MRI techniques derive their contrast through differences in phase accrual caused by motion: flow imaging, phase-contrast angiography (PC-MRA), magnetic resonance elastography (MRE), etc. These techniques rely on motion sensitizing gradient pulses, which for diffusion are called diffusion encoding gradient (DEG) waveforms.

The first diffusion measurements using the principle of nuclear magnetic resonance (NMR) were performed by Carr and Purcell in 1954 (4) and improved by Stejskal and Tanner in 1965 (5). A method to spatially encode the NMR signal was devised by Lauterbur in 1973 (6), giving rise to MRI. The first *in vivo* diffusion-weighted imaging (DWI) experiments were performed by Le Bihan and Breton in 1985 (7,8). Tremendous improvements in imaging speed through hardware improvements and introduction of new techniques, such as echoplanar imaging (9–11), allowed to overcome motion artifacts plaguing diffusion MRI. This eventually led to the development of diffusion tensor imaging (DTI) in 1994 (12), enabling three-dimensional diffusion models (13).

Together these advancements made possible the clinical adoption of diffusion MRI methods and enabled new applications. For example, changes in tissue structure affecting diffusion, such as the proportion of intra- and extracellular space, are observed during carcinogenesis. Different cancer types and developmental stages of tumors display contrasting diffusion properties. This allows classification of tumors based on acquired diffusion-weighted images, which is further enhanced by other contrast mechanisms, such as T_1 - and T_2 -weighting, and other imaging modalities (14).

Some of the many applications of diffusion MRI in oncology are (15): differentiation and grading of neoplastic lesions in the brain, planning radiation therapy volumes in glioblastoma treatment, adenocarcinomas in the breast and prostate, and characterization of hepatocellular carcinoma in the liver and extrahepatic metastases in lymph nodes and pancreas. Evaluation of liver cirrhosis

or fibrosis has also been performed alone and in combination with MRE (16). Cerebral infarctions and hemorrhages have been studied (14,17). DWI has been applied in the heart to characterize myocardial infarction (18) and detect fibrosis in chronic cardiomyopathy (19).

White matter and neurodegenerative diseases, such as Alzheimer's, Parkinson's and multiple sclerosis, can be diagnosed in early stages using DTI (20), which has also been found to be a powerful tool to study pediatric brain development (21). A major application of DTI is tractography, where the orientation of fiber tracts in nerve or muscle tissues is tracked based on the principal direction of diffusion in each voxel. This has led to the development of connectomics, a discipline studying neuronal connectivity (22–24). DTI based tractography has also been applied to examine myocardial structure (25–27).

1.2 Challenges in Diffusion MRI

On the typical timescale of diffusion encoding in MRI (up to $\sim 100\text{ ms}$) self-diffusion of water molecules in tissues is on the order of $\sim 10\text{ }\mu\text{m}$. To increase sensitivity to such small displacements, strong magnetic field gradients are necessary. Increasing the encoding time, i.e. applying DEGs over a longer time period, can also increase contrast. Due to exponential signal attenuation after a resonant excitation of nuclear spins, longer intervals until signal readout inherently lead to lower signal amplitudes, whereas noise remains relatively constant. In a spin echo (28) acquisition as is commonly used in all clinical diffusion MRI, the duration between excitation and readout is called echo time (TE).

The signal-to-noise ratio (SNR) is a crucial metric for all MRI techniques. It is necessary not only to achieve high contrast, but sufficient SNR is required as well (29). Most noise in diffusion MRI is intrinsic and originates from the tissue or sample investigated. Less significant noise sources include thermal noise in transmit/receive coils and gradient amplifier electronics, mechanical vibrations, and external interferences. MRI methodology development is largely reliant on signal gains to improve SNR while keeping scan durations short, hence the motivation to reduce TE for diffusion scans.

Another important aspect is motion robustness. Sequences with long diffusion encoding are prone to motion artifacts such as ghosting and blurring (30). Special DEG waveforms have been developed to compensate for bulk motion (31–33). Three-dimensional imaging and acquisition of several diffusion directions is challenging since movement between repetitions causes data inconsistencies. The overall imaging time can be reduced using parallel imaging techniques such as SENSE in image domain (34) or GRAPPA in k -space (35). Furthermore, it is possible to use gating methods where the acquisition start is synchronized with respiration using a respiratory belt, the cardiac cycle using ECG as a trigger signal, or both, through which the acquisition can be synchronized with periods of reduced motion. The acquisition can also be synchronized using the MR signal itself, which is called self-gating or navigation (36–38). A further method to mitigate the effects of motion on measurements is to utilize a stimulated echo sequence, preserving the encoding between separate cardiac cycles, but this method suffers from inherently low SNR (39). Development of diffusion imaging applications for cardiovascular magnetic resonance imaging (CMR) is particularly difficult and it is essential to combine several methods to reduce motion sensitivity, including rapid diffusion encoding.

A significant difficulty in tractography is distinguishing true structure in areas with crossing fibers (40), as displayed in Figure 1.1 below. It occurs when fiber populations of different directions are present in a single voxel, and is caused by the inability of DTI to fully quantify individual components of diffusion in such areas due to the statistical nature of the attenuation effect (1,41). Such a situation is commonly encountered in white matter tracts in the brain, where implemented fiber-tracking methods fail, resulting in both false positive non-anatomical tracts and true negatives, i.e. failing to capture anatomical tracts (42). This is caused by the immense complexity of neuronal pathways on several scales and cannot be fully solved by increasing resolution (43) or number of diffusion encoding directions used to reconstruct the diffusion tensor (44). However, it is still useful to increase spatial and angular resolution since these can be used to build finer structural models (45) that can be analyzed on several scales and allowing more complex diffusion models, such as diffusion spectra or orientation distribution functions (25,46), and tractographic reconstruction methods (24). To increase spatial resolution of fast EPI readouts employed with diffusion image acquisitions, it is beneficial to increase the readout duration. This can only be achieved with reasonable SNR if the diffusion encoding is sufficiently short, such that the amplitude of the spin echo signal has not yet decayed due to spin-spin interactions.

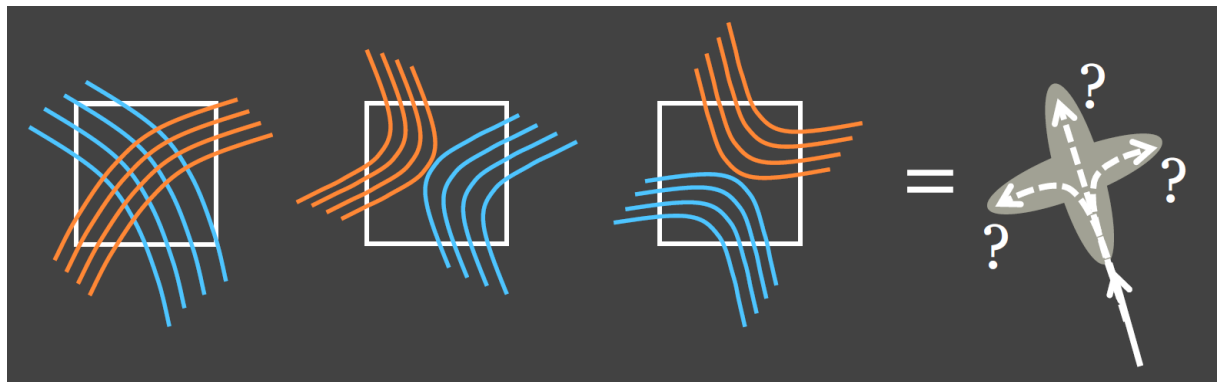


Figure 1.1: Ambiguity of crossing fibers within a single voxel. Image source: (47)

A straightforward method to increase encoding efficiency is to increase the DEG amplitude and gradient duty cycle. Clinical MR systems have a gradient strength up to 80 mT/m , with strengths of 40 mT/m or less per gradient axis being far more common. Beginning in 2009, the Human Connectome Project (HCP) has made a large-scale effort to describe functional connections in the human brain with unprecedented acuity using DTI tractography (22,23). To this purpose, a specialized MR system was developed in order to achieve extremely large gradient amplitudes. The Siemens Magnetom Skyra Connectom system was constructed with four overlapping gradient coils per axis, driven by separate amplifiers. Each coil achieves 75 mT/m amplitudes for a total gradient strength of 300 mT/m per axis. The slew rate is de-rated to 62.5 T/m/s to avoid physiological stimulation during diffusion encoding. All experiments and data presented in this work were performed on the Connectom scanner located at the Massachusetts General Hospital (MGH) in Boston, Massachusetts.

Higher gradient strengths exacerbate effects of gradient imperfections on diffusion imaging. The primary perturbations arise from eddy-current (1,48) and concomitant gradient fields (2,49). Another source are gradient non-linearities and calibration errors (50).

1.3 Gradient Waveform Optimization

Pulse sequences define the MR experiment. They are named after the RF and gradient pulses that are used to selectively excite and spatially encode the spin signal. Despite the name, it is an artificial restriction to require trapezoidal gradient pulses for this purpose. It is a severe restriction of the MR parameter space that can exclude optimal solutions for a given imaging problem. Mathematical optimization methods have been employed to design pulse sequences that are not bound to such restrictions (51–55). Optimization approaches have also been applied to improve diffusion encoding (56–59).

Diffusion encoding gradient waveforms are designed to refocus all phase effects for stationary spins, while diffusing spins experience a different field history due to their motion and hence do not fully refocus. The most obvious method to attain this is to use a design that is symmetric around a refocusing or inversion RF pulse. Such a symmetric gradient waveform also refocuses stationary spins if the gradients are imperfect, i.e. we expect the same erroneous gradient behavior in the first waveform part and the second after the inversion, which then cancels out. In this way, gradient non-linearities, eddy-currents and concomitant gradient fields are effectively corrected.

Symmetric DEG waveforms rely on precise 180° echo pulses without phase distortions and defects, i.e. they are susceptible to B_1 imperfections. Furthermore, long idle periods without gradient pulses are needed for long EPI readout durations in order to align the EPI train with the spin echo center. This reduces gradient encoding efficiency and increases required TE. Alternatively, the readout duration is reduced since the gradient waveform must be the same length before and after the inversion, limiting attainable resolution. Some of these problems have been successfully addressed with asymmetric waveform designs (3,60,61). The employed DEGs, before and after the inversion, produce the same displacements in k -space but do not traverse the same trajectory. Asymmetric DEG waveforms are less constrained in form, making it comparatively more difficult to create sequences fitting the desired parameters. This necessitates numerical optimization approaches to find matching solutions. Compared to symmetric designs, these do not inherently correct undesired gradient effects, requiring more careful design considerations to specifically address and compensate these inaccuracies.

The objective of this thesis is to investigate the benefits of using asymmetric waveforms to encode diffusion in an efficient and robust manner. The work conducted aims to increase imaging resolution by reducing the echo time and increasing readout durations of spin echo diffusion encoding sequences. To this end, a waveform optimization framework was developed and used to design concomitant-compensated (COCO) sequences for diffusion imaging matching desired criteria. The following chapters introduce the underlying theory, present the developed optimization framework and methodology used to compare and evaluate the obtained waveforms, as well as a detailed analysis of results obtained from imaging experiments comparing the new method against older methods.

2 Theory

2.1 Diffusion MRI Basics

2.1.1 Physics of Molecular Diffusion

Diffusion (from Latin *diffundere*, “to spread” or “to extend”) is a mass transport phenomenon whereby particles in areas with a higher concentration gradually spread to areas of lower concentration. This is driven by a gradient in chemical potential and brought about by random walks of small particles, in this case molecules, termed *Brownian Motion*.

This contrasts with bulk motion, or advection, in which a net flow is transported in a directed rather than a random fashion. Diffusive processes are governed by Fick’s First Law, which establishes a relation between diffusion flux \mathbf{J} and substance concentration c :

$$\mathbf{J}(\mathbf{r}, t) = -D \nabla c(\mathbf{r}, t) \quad [2.1]$$

Here, D is the diffusion coefficient or mean free diffusivity, which is a measure of the rate at which an equilibrium concentration level is attained. The diffusion flux is subject to a continuity relation:

$$\nabla \cdot \mathbf{J}(\mathbf{r}, t) = -\frac{\partial c(\mathbf{r}, t)}{\partial t}, \quad [2.2]$$

which together gives Fick’s Second Law, better known as the diffusion equation (62):

$$\frac{\partial c(\mathbf{r}, t)}{\partial t} = \nabla \cdot D \nabla c(\mathbf{r}, t) \quad [2.3]$$

If the initial concentration of molecules is homogeneous, there exists no chemical potential gradient to drive diffusion resulting in zero net flux. However, the molecular thermal motion is still present and is described by the same underlying principles governing Brownian motion. This process is called *self-diffusion*. Rather than observing the concentration of molecules diffusing, we look at the probability of finding a particle at a particular distance from the starting point after a specific time, which is given as a probability density function $P(\mathbf{r}, t)$ known as a *propagator* (46). The corresponding probability density flux obeys the equivalent Fokker-Planck equation:

$$\frac{\partial P(\mathbf{r}, t)}{\partial t} = \nabla \cdot D \nabla P(\mathbf{r}, t) = D \nabla^2 P(\mathbf{r}, t) \quad [2.4]$$

In its form, equation 2.4 is a common partial differential equation and is equivalent to the heat equation in thermodynamics. For an instantaneous point-like source, $P(\mathbf{r}, t_0) = \delta(\mathbf{r} - \mathbf{r}_0)$, the special case solution, i.e. the impulse response of the system, is given by a series of isotropically dispersing Gaussian distributions centered at \mathbf{r}_0 (63), as shown in Figure 2.1. This solution can be described by the following function:

$$P(\mathbf{r}, t) = \frac{1}{(4\pi D(t - t_0))^{3/2}} \exp\left(-\frac{\|\mathbf{r} - \mathbf{r}_0\|_2^2}{4D(t - t_0)}\right) \quad [2.5]$$

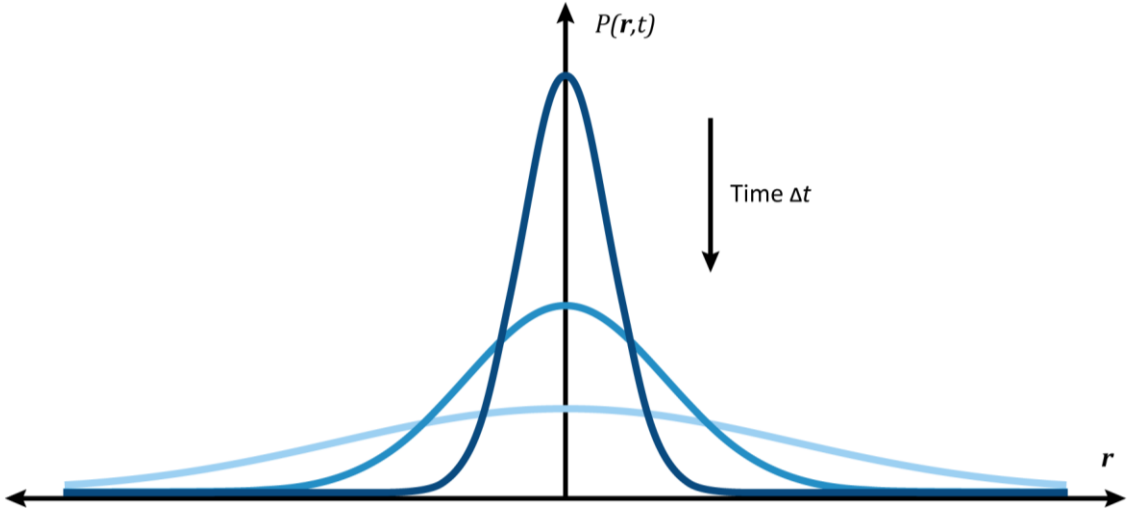


Figure 2.1: Evolution of probability distributions in one dimension for $\mathbf{r}_0 = 0$. Unconstrained Brownian motion can be described through the gradual broadening of a Gaussian distribution giving the probability of finding the diffusing particle at some distance from the starting point. Adapted from: (63)

If we calculate the moments of this distribution, the zeroth moment gives the total probability, which is equal to 1. The first moment is the mean of the normal distribution, in this case the starting point r_0 . The second moment is given by the variance of the distribution and is equal to the mean square displacement of the particles, known as the mean free path. We obtain the following expressions:

$$\mu_0 = \int_{-\infty}^{\infty} P(\mathbf{r}, t) dr = 1 \quad [2.6]$$

$$\mu_1 = \int_{-\infty}^{\infty} P(\mathbf{r}, t) \mathbf{r} dr = \mu = r_0 \quad [2.7]$$

$$\mu_2 = \int_{-\infty}^{\infty} P(\mathbf{r}, t) \mathbf{r}^2 dr = \sigma^2 = 6D(t - t_0) = \|\mathbf{r} - \mathbf{r}_0\|_2^2 \quad [2.8]$$

The resulting expression for the free diffusion coefficient in a homogeneous isotropic medium is known as the Einstein-Smoluchowski relation:

$$D = \frac{\|\mathbf{r} - \mathbf{r}_0\|_2^2}{6(t - t_0)} = \frac{\overline{\Delta r^2}}{6\Delta t} \quad [2.9]$$

2.1.2 Magnetization Evolution

Throughout the work, directions are given in a three-dimensional orthogonal coordinate system, with the z direction aligned with the static magnetic field B_0 , while the x and y directions point radially outward from the bore axis. The evolution of magnetization is governed by the Bloch equations (64), which for the given coordinate system can be represented in vector notation:

$$\frac{d\mathbf{M}_{Bloch}(t)}{dt} = \gamma \mathbf{M}_{Bloch}(t) \times \mathbf{B}(t) - \begin{pmatrix} \mathbf{M}_{xy}/T_2 \\ (M_z - M_0)/T_1 \end{pmatrix} \quad [2.10]$$

If only the principal magnetic component B_0 is present during the spin evolution, the solution to equation 2.10 is given by a transversal precession and spin-spin relaxation, and a longitudinal spin-lattice recovery:

$$\mathbf{M}_{Bloch}(t) = \begin{pmatrix} \mathbf{M}_{xy}(t) \\ M_z(t) \end{pmatrix} = \begin{pmatrix} \mathbf{M}_{xy}(0) e^{-i\gamma B_0 t} e^{-t/T_2} \\ M_0 + (M_z(0) - M_0) e^{-t/T_1} \end{pmatrix} \quad [2.11]$$

where $M_{xy} = M_x - iM_y$ is the transversal magnetization component and M_0 is the equilibrium magnetization. This was expanded by Torrey to include a diffusion term, giving the Bloch-Torrey equation (65):

$$\frac{d\mathbf{M}(t)}{dt} = \gamma \mathbf{M}(t) \times \mathbf{B}(t) - \begin{pmatrix} \mathbf{M}_{xy}/T_2 \\ (M_z - M_0)/T_1 \end{pmatrix} + \nabla \cdot D \nabla (\mathbf{M}(t) - \mathbf{M}_0) \quad [2.12]$$

For a spatially-varying magnetic field, the additional term causes an exponential attenuation dependent on the diffusion coefficient and a so called b -value (8):

$$\mathbf{M}(t) = \mathbf{M}_{Bloch}(t) e^{-bD} \quad [2.13]$$

Higher gradient strengths and longer diffusion encoding result in a higher contrast diffusion weighted image; however, as signal decays exponentially a tradeoff needs to be made. For an MR diffusion experiment the b -value is typically chosen such that the contrast-to-noise ratio (CNR) is maximized (29). A simple rule of thumb that can be employed is to choose a b -value according to the tissue being characterized such that $D \cdot b \approx 1$.

2.1.3 Diffusion Encoding Gradient Waveforms

Erwin Hahn conducted the first NMR spin echo (SE) experiments in 1950 (28). This formed the base for many consequently developed pulse sequences in common use today. In SE sequences an RF pulse is followed by one or multiple further pulses which partially refocus spins dephased due to magnetic field inhomogeneities with a $1/T_2^*$ dependence, inducing stimulated echoes at the echo time TE . The maximum echo amplitude is achieved using a combination of a 90° excitation pulse followed by a 180° echo pulse (4). Assuming stationary inhomogeneities and spins, such a sequence produces exponentially decaying echo amplitudes with decay rate given by $1/T_2$.

If spins are not stationary and experience a different field history before and after the echo pulse, the spins will not refocus fully, leading to an attenuated echo signal. This signal difference is the basis for diffusion contrast in MRI. The stochastic motion of excited spins due to thermal self-diffusion of water molecules causes a signal attenuation dependent on the diffusivity of surrounding tissue. Local field inhomogeneities are small over typical diffusion lengths of water in tissue, resulting in a negligible attenuation effect. This can be amplified by applying strong diffusion sensitizing gradients, hence introducing large spatial field variations. If field gradients are applied before and after the echo pulse, non-stationary spins accrue a phase which increases with gradient strength and distance traveled along the spatial field variation, as seen in Figure 2.2 below.

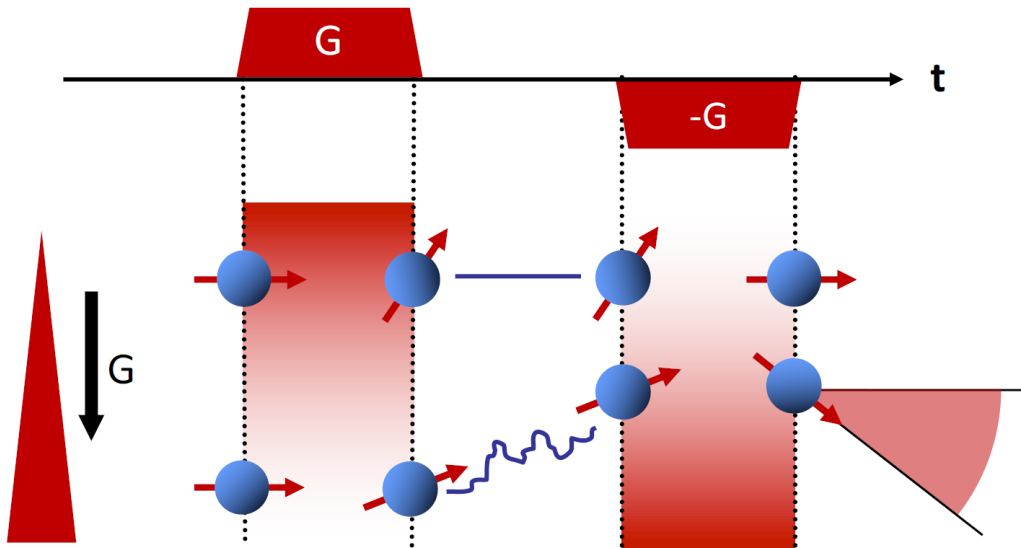


Figure 2.2: MRI phase evolution of diffusing vs. stationary spins. During the second gradient pulse, spins that have diffused in a direction along the field gradient will not experience the same pulse strength and will have a remaining phase shift after the refocusing pulse, contributing to signal attenuation during the ensuing readout. Image source: (66)

The phase accrued during this process is given by:

$$\phi(TE) = \gamma \int_0^{TE} B_0 + \mathbf{G}(t) \cdot \mathbf{r}(t) dt \quad [2.14]$$

In 1965, Stejskal and Tanner (5) first employed a pulsed gradient spin echo sequence (PGSE) to induce a diffusion-weighted attenuation along a particular encoding direction in an NMR signal. It utilized a symmetric gradient pulse pair placed on both sides of the echo pulse; the sequence diagram is given in Figure 2.3.

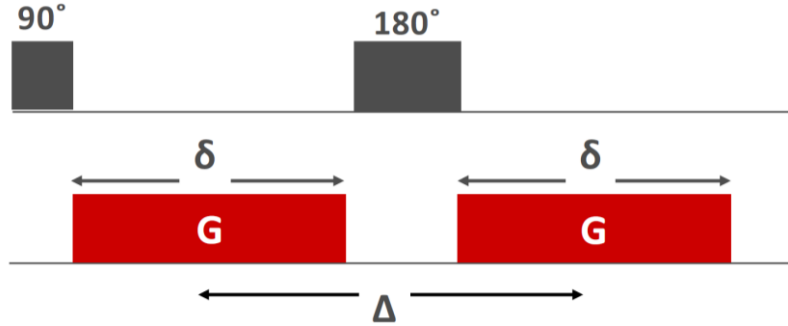


Figure 2.3: Stejskal-Tanner pulse sequence diagram. Image source: (66)

The ratio of acquired signal strengths in such an experiment with and without diffusion encoding is then given by (8):

$$\frac{S_{ST}}{S_0} = \exp\left(-\gamma^2 G^2 \delta^2 \left(\Delta - \frac{\delta}{3}\right) D\right) = e^{-bD} \Rightarrow b = \gamma^2 G^2 \delta^2 \left(\Delta - \frac{\delta}{3}\right) \quad [2.15]$$

We can generalize the gradient waveform to any desired shape and direction. The field gradient $\mathbf{G}(t) = (G_x(t) \quad G_y(t) \quad G_z(t))^T$ is given by the components of the applied magnetic field gradients along each of the principal axes, where the notation indicates spatial variation in the spatial coordinates of a magnetic field parallel to the static magnetic field B_0 in the z direction. For the diffusion preparation period t_{diff} , we obtain an expression for evaluation of diffusion encoding sensitivity given by the b -value:

$$b = \int_0^{t_{diff}} \mathbf{k}(t) \cdot \mathbf{k}(t) dt, \quad \text{where } \mathbf{k}(t) = \int_0^t \mathbf{G}(\tau) \operatorname{sgn}(t_{inv} - \tau) d\tau \quad [2.16]$$

The combination of a readout sequence with spatial encoding of the diffusion signal eventually gave rise to *diffusion-weighted imaging* (DWI). An echoplanar imaging (EPI) readout is used most commonly in conjunction with diffusion weighting. Diffusion encoding waveforms are typically symmetric around the echo pulse, but asymmetric designs can be employed as well, as long the phase of stationary spins is refocused at the end of the diffusion encoding.

The outline of a diffusion encoding spin echo sequence with corresponding timings is provided in Figure 2.4. Important durations and timepoints in the sequence are: preparation time t_{pre} which includes half the excitation pulse duration t_{90} , any navigator acquisitions, EPI correction lines and refocusing lobes; encoding time t_{enc} encompassing the full time from the start of the diffusion encoding till the end; mixing time t_{mix} to increase diffusion sensitivity of M_0 -nulled symmetric sequence; echo pulse duration t_{RF} ; timepoint of inversion t_{inv} at the center of the echo pulse, given in relation to the excitation; deadtime t_{post} after diffusion encoding and before start of the readout; readout duration $t_{read} = 2 t_{EPI}$; and echo time TE centered at the readout. The start- and endpoint of the echo pulse are defined as $t_{RF^-} = t_{inv} - t_{RF}/2$ and $t_{RF^+} = t_{inv} + t_{RF}/2$, respectively.

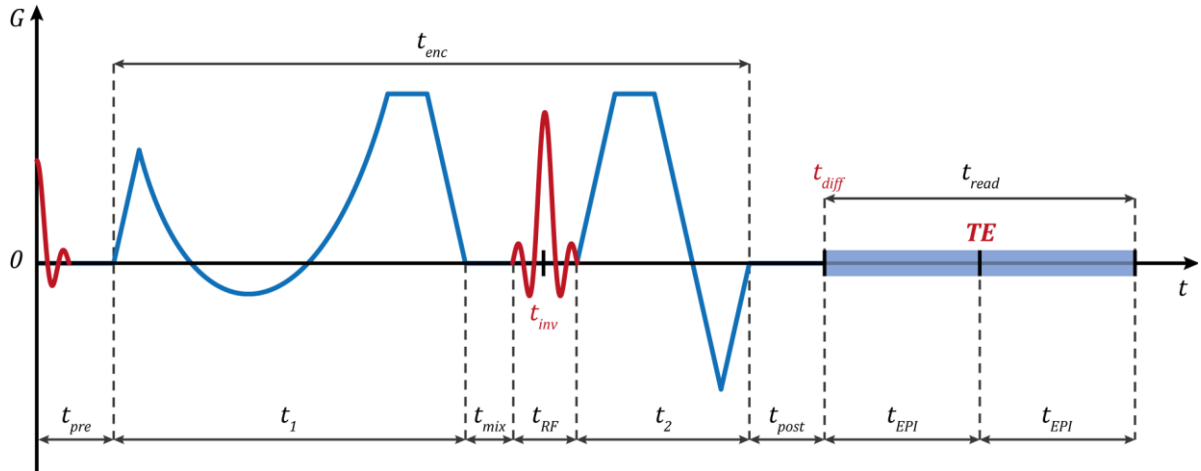


Figure 2.4: Depiction of DWI spin echo pulse sequence using an arbitrary asymmetric gradient waveform. Relevant durations are noted on the graph. Important timepoints, given relative to the start of the spin echo sequence with the excitation pulse, are marked in red.

2.2 Diffusion Metrics and Visualization

2.2.1 Diffusion-Weighted Imaging (DWI)

In biological tissue, diffusion is affected by a range of factors, including tissue structure and biological function, and hence does not behave exactly as a Gaussian diffusion process described above. In magnetic resonance measurements, the signal is also affected by intravoxel incoherent motion (IVIM), such as blood circulation in small vessels, and cerebrospinal fluid pulsation (8,15). Additionally, due to the resolution and other methodological limitations, it is not possible to determine the pointwise exact diffusion coefficient; rather a mean value over the voxel is measured. The *apparent diffusion coefficient* (ADC) is introduced to reflect these inherent limitations (67). Table 2.1 shows the range of typically measured average ADC values measured in a variety of tissues in healthy adults.

Tissue / Material	ADC Value [$\times 10^{-3} \text{ mm}^2/\text{s}$]	b-value [s/mm^2]	Source
Free water (20°C)	2.025 ± 0.005	N.A.	Holz et al. (68)
Free water (25°C)	2.299 ± 0.005	N.A.	Holz et al. (68)
Brain	0.71 ± 0.01	100	Peña-Nogales et al. (61)
Spinal Cord	0.976 ± 0.19	$0 - 1000$	Kolff-Gart et al. (69)
Myocardium	1.4 ± 0.2	350	Nguyen et al. (70)
Liver	1.53 ± 0.21	500	Peña-Nogales et al. (61)

Table 2.1: Typical ADC values of biological tissues and water. The values for tissue are compiled from a variety of sources based on *in vivo* measurements of healthy tissue regions. The measurements are given with the b-value at which these were acquired, since the information is relevant for interpretation (67).

The ADC value can be calculated from two individual measurements with different b -values, a method which also corrects for differences in T_2 relaxation in the tissue, preventing the effect of so-called T_2 shine-through (29):

$$ADC = -\frac{\ln(S_1/S_0)}{b_1 - b_0} \quad [2.17]$$

In DWI, diffusion is encoded along the direction of the applied DEG fields. A different ADC value results for each direction, depending on the tissue structures restricting free diffusion along the inspected direction, i.e. we would observe a large ADC value in the direction of a fiber structure and reduced radial values. The diffusion-weighted signal acquired in three orthogonal directions is given by the vector \mathbf{S} :

$$\mathbf{S} = \begin{pmatrix} S_x \\ S_y \\ S_z \end{pmatrix} = S_0 \begin{pmatrix} e^{-b \text{ } ADC_x} \\ e^{-b \text{ } ADC_y} \\ e^{-b \text{ } ADC_z} \end{pmatrix} \quad [2.18]$$

The mean diffusion-weighted signal S_{DWI} is given by the geometric mean of the individual components:

$$S_{DWI} = \sqrt[3]{S_x S_y S_z} = S_0 e^{-b(ADC_x + ADC_y + ADC_z)/3} \quad [2.19]$$

The mean diffusivity (MD) and trace diffusivity values are then given by the following relation, which is the same for acquisition along any set of three orthogonal directions:

$$MD = \bar{\lambda} = \frac{ADC_{trace}}{3} = \frac{1}{3}(ADC_x + ADC_y + ADC_z) \quad [2.20]$$

2.2.2 Diffusion Tensor Imaging (DTI)

In tissues, diffusion is rarely isotropic and cannot be fully described by a constant scalar value. Physical structures such as vessel walls, nerve fascicles, and muscle fibers impose barriers to the self-diffusion of water. To incorporate anisotropic diffusion effects into the Gaussian model, an extension is introduced (12). The diffusion properties are modeled by a *diffusion tensor* rather than a scalar coefficient:

$$\mathbf{D} = \begin{pmatrix} D_{xx} & D_{xy} & D_{xz} \\ D_{yx} & D_{yy} & D_{yz} \\ D_{zx} & D_{zy} & D_{zz} \end{pmatrix} \quad [2.21]$$

Off-diagonal elements are zero for isotropic diffusion, and the diffusion trace weighting is given by $ADC_{trace} = \text{trace}(\mathbf{D})$. The diffusion tensor is a symmetric positive-definite 3×3 matrix. An extension of the b -value as derived for DWI in equation 2.16 is given by the b -matrix (71):

$$\mathbf{b} = \gamma^2 \int_0^{t_{diff}} \mathbf{k}(t) \otimes \mathbf{k}(t) dt \quad [2.22]$$

This is a symmetric 3×3 matrix describing diffusion encoding along each axis caused by each field gradient axis. At least six different diffusion encoded acquisitions in non-collinear diffusion directions and an additional acquisition S_0 without encoding must be made to calculate all tensor elements, which is achieved using an appropriate gradient encoding scheme (13). The diffusion tensor can be reconstructed by setting up and solving a set of equations resulting from the individual acquisitions with encoding characterized by \mathbf{b}^n :

$$\ln\left(\frac{S(\mathbf{b}^n)}{S_0}\right) = -\sum_{i=1}^3 \sum_{j=1}^3 b_{ij}^n D_{ij} \quad [2.23]$$

Once the system is solved, several useful metrics can be derived from the diffusion tensor. Due to symmetry of the diffusion tensor, the eigendecomposition is orthonormal and given by:

$$\mathbf{D} = (\mathbf{v}_1 \quad \mathbf{v}_2 \quad \mathbf{v}_3) \begin{pmatrix} \lambda_1 & 0 & 0 \\ 0 & \lambda_2 & 0 \\ 0 & 0 & \lambda_3 \end{pmatrix} (\mathbf{v}_1 \quad \mathbf{v}_2 \quad \mathbf{v}_3)^{-1} = \mathbf{P} \boldsymbol{\Lambda} \mathbf{P}^{-1} = \mathbf{P} \boldsymbol{\Lambda} \mathbf{P}^T \quad [2.24]$$

A diffusion tensor can be visualized by an ellipsoid whose axes lengths are determined by the inverse root of its eigenvalues, given as the diagonal entries of $\boldsymbol{\Lambda} = \text{diag}(\lambda_1, \lambda_2, \lambda_3)$. The orientation of the ellipsoid is given as a rotation of the principal coordinate axes $\mathbf{r} = (x \ y \ z)$ by the matrix composed of the eigenvectors $\mathbf{P} = (\mathbf{v}_1 \quad \mathbf{v}_2 \quad \mathbf{v}_3)$. The diffusion ellipse and the interpretation of the eigenvalue decomposition leading to the ellipse parameters is depicted graphically in Figure 2.5. Such an ellipsoid satisfies the following equality:

$$\mathbf{r} \mathbf{D} \mathbf{r}^T = \mathbf{r} \mathbf{P} \boldsymbol{\Lambda} \mathbf{P}^T \mathbf{r}^T = \left(\frac{\mathbf{r} \mathbf{v}_1}{\sqrt{\lambda_1}}\right)^2 + \left(\frac{\mathbf{r} \mathbf{v}_2}{\sqrt{\lambda_2}}\right)^2 + \left(\frac{\mathbf{r} \mathbf{v}_3}{\sqrt{\lambda_3}}\right)^2 = 1 \quad [2.25]$$

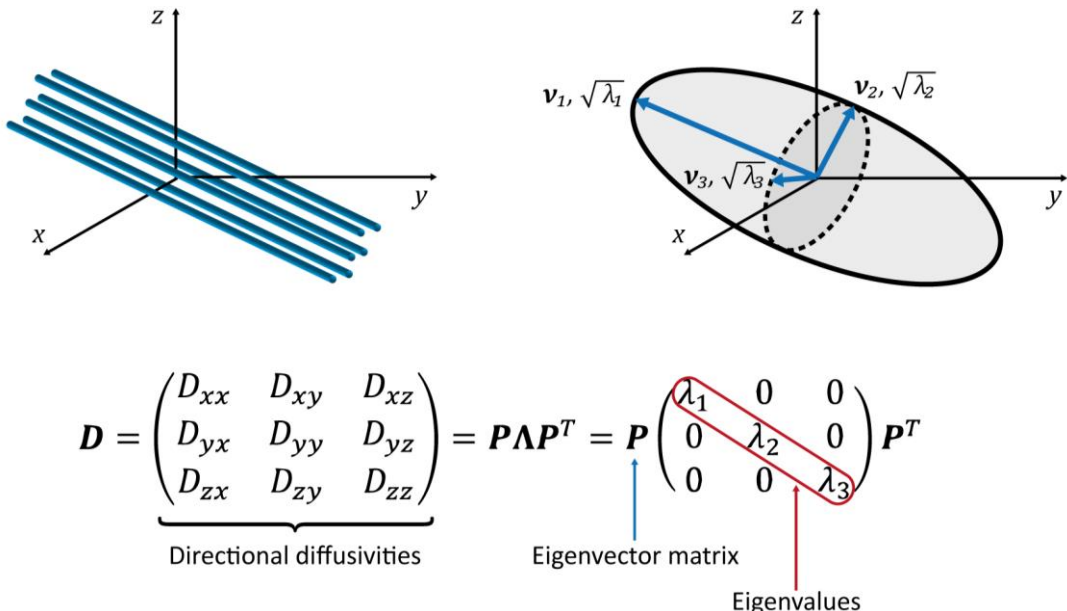


Figure 2.5: Diffusion tensor visualization. The diffusion tensor can be depicted as an ellipsoid with principal axes oriented along the eigenvectors \mathbf{v}_1 , \mathbf{v}_2 and \mathbf{v}_3 and length given by the eigenvalues of \mathbf{D} . The orientation of the ellipsoid is correlated to the orientation of fibers in the measured object. Adapted from: (72)

An ellipse can be characterized according to its axis proportions by its linearity, planarity, and sphericity, or conversely by its anisotropy. These relations are given by:

- Linearity:

$$c_l = \frac{\lambda_1 - \lambda_2}{\lambda_1 + \lambda_2 + \lambda_3} \quad [2.26]$$

- Planarity:

$$c_p = \frac{2(\lambda_2 - \lambda_3)}{\lambda_1 + \lambda_2 + \lambda_3} \quad [2.27]$$

- Sphericity:

$$c_s = \frac{3\lambda_3}{\lambda_1 + \lambda_2 + \lambda_3} \quad [2.28]$$

- Anisotropy:

$$c_a = 1 - c_s = c_l + c_p \quad [2.29]$$

Further scalar metrics can be established to classify diffusion tensors by their defining ellipsoid's shape and eccentricity, establishing measures to quantify the degree of anisotropy. The fractional anisotropy has values in the range $[0,1]$, where 0 describes isotropic diffusion and 1 a diffusive process perfectly restricted along a single direction. Relative anisotropy similarly describes the anisotropy in the range $[0, \sqrt{2}]$. The volume ratio is defined as the ratio between the volume of the ellipsoid and a sphere with the same trace diffusivity. These are listed below:

- Fractional Anisotropy:

$$FA = \sqrt{\frac{3}{2} \frac{(\lambda_1 - \bar{\lambda})^2 + (\lambda_2 - \bar{\lambda})^2 + (\lambda_3 - \bar{\lambda})^2}{\lambda_1^2 + \lambda_2^2 + \lambda_3^2}} \quad [2.30]$$

- Relative Anisotropy:

$$RA = \sqrt{\frac{(\lambda_1 - \bar{\lambda})^2 + (\lambda_2 - \bar{\lambda})^2 + (\lambda_3 - \bar{\lambda})^2}{3\bar{\lambda}}} \quad [2.31]$$

- Volume Ratio:

$$VR = \frac{\lambda_1 \lambda_2 \lambda_3}{\bar{\lambda}^3} \quad [2.32]$$

2.3 Gradient Effects

2.3.1 Gradient Moments

Concurrent field gradients and bulk motion in a spin echo sequence result in an additional phase shift ϕ_m . Performing a Taylor expansion of the position at the starting point in the expression for the accrued phase, we obtain:

$$\begin{aligned} \phi_m(TE) &= \gamma \int_0^{TE} \mathbf{G}(t) \cdot \mathbf{r}(t) dt = \gamma \int_0^{TE} \mathbf{G}(t) \cdot \left(\mathbf{r}(0) + t\dot{\mathbf{r}}(0) + \frac{t^2}{2}\ddot{\mathbf{r}}(0) + \dots \right) dt = \\ &\underbrace{\mathbf{r}_0 \cdot \left(\gamma \int_0^{TE} \mathbf{G}(t) dt \right)}_{M_0} + \underbrace{\mathbf{v}_0 \cdot \left(\gamma \int_0^{TE} t\mathbf{G}(t) dt \right)}_{M_1} + \underbrace{\mathbf{a}_0 \cdot \left(\frac{\gamma}{2} \int_0^{TE} t^2 \mathbf{G}(t) dt \right)}_{M_2} + \dots \end{aligned} \quad [2.33]$$

The total phase accrued due to bulk motion can be approximated to the second order by adding the contributions of the position \mathbf{r}_0 , velocity \mathbf{v}_0 , and acceleration \mathbf{a}_0 immediately after excitation, multiplied by gradient moments of the respective order. The accrued phase ϕ_m affects phase-encoding of the EPI readout, causing blurring and ghosting artifacts. Crusher gradients can be employed to destroy unwanted transversal phase; this causes a signal fallout with a $\cos \phi_m$ dependence, and causes misestimation in the measurement (73).

Compensating bulk motion effects is crucial for accurately measuring diffusion processes in the body, especially when imaging areas of the body typically affected by motion artifacts, such as the heart and abdominal organs which are susceptible to respiratory motion. Quiescent cardiac motion is roughly on the order of $\bar{v} = 0.015 \text{ m/s}$ and $\bar{a} = 0.1 \text{ m/s}^2$, while peak motion is around an order of magnitude larger (70,74).

Several gradient encoding sequences have been developed to compensate for bulk motion in MR diffusion measurements by nulling gradient moments. Such sequences most commonly utilize trapezoidal gradient lobes and are symmetric around the RF echo pulse. When a single monopolar (1,1) pulse pair of equal area is used, M_0 -nulling is achieved. Higher moment orders can then be compensated if more lobes are added and their shape is modified. Using a bipolar (1,-1,1,-1) pulse pair around an echo pulse, with each side individually being M_0 -nulled, we obtain an M_0 and M_1 -nulled or flow-compensated sequence. A (1,-2,-2,1) pulse order allows additional M_2 -nulling. These symmetric sequences are referred to as MONO (8), BIPOLE (32) and MOCO (31), respectively. A schematic overview of each is shown in Figure 2.6. For simplicity, M_1 -nulling are implicitly used to signify both M_0 and M_1 -nulled DEG waveforms, whereas M_2 -nulled sequences imply waveforms which are M_0 , M_1 and M_2 -nulled.

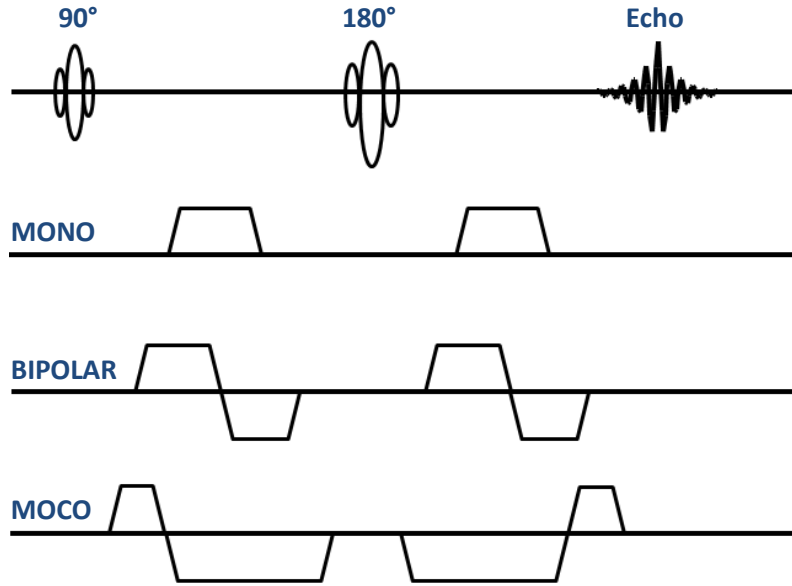


Figure 2.6: Symmetric diffusion encoding sequences. MONO implements an M_0 -nulled diffusion encoding with a monopolar pulse pair. BIPOLAR utilizes a bipolar pulse pair and achieves M_0 - and M_1 -nulling. MOCO compensates bulk motion up to the second order through a modified bipolar antisymmetric pulse pair. Adapted from: (75)

Third and higher order gradient moment nulling can be accomplished (76), but is not of interest in this work. However, analysis of gradient moment evolution during diffusion encoding allows to infer upon the motion sensitivity in various points of the sequence. Particularly large spikes in a gradient moment at specific points can indicate a sensitivity to higher order motion.

2.3.2 Eddy Currents

Rapidly switching magnetic field gradient are required to spatially encode signal information in MRI. The changes in magnetic flux associated with the switching induce electric currents in conducting structures such as the gradient, shim, and RF-transmit/receive coils (77). Given the nature of Faraday's law, these will be circular currents in planes perpendicular to the applied field that eventually dissipate due to losses. These currents in turn induce a magnetic field which according to Lenz's law counteracts the change in field. During the initial stage of switching, these effects can be so large that they cause an apparent overall delay in gradient response. In an MR system, eddy currents are often modeled using a lumped LR-circuit analogy which gives the characteristic multi-exponential decay observed in the gradient response (78,79). The effect on the gradient waveforms can be described by a convolution of the desired waveform by an impulse response modeled as a sum of exponential decay terms of different time-constants.

For imaging, pre-emphasis correction is frequently employed to minimize eddy current effects. Due to the large field gradient present during diffusion encoding, even small remaining effects can be detrimental to image quality. Attempts to design DEG waveforms have been successful at nulling eddy-currents of a single time-constant (58,60). Comprehensive measurement and correction of eddy-currents for diffusion MRI can be performed with different means, such as through prospective mapping for post-processing correction (48,80) or concurrent field monitoring (81–83).

2.3.3 Concomitant Gradient Fields

Concomitant fields are a by-product of the attempt to create the specifically desired field configurations common in MR experiments, an overlap of a spatially homogeneous B_0 field, and linearly varying field gradient \mathbf{G} oriented along the bore in the z direction. Such a field configuration necessarily has an additional concomitant field configuration, which together satisfy Maxwell's equations (49,84), thus also being known as Maxwell fields. Assuming there are no current sources inside the field distribution the curl of the field \mathbf{B} is zero ($\nabla \times \mathbf{B} = 0$), which cannot hold true if there is a gradient in a single direction. Assuming the field gradients are spatially symmetric around the isocenter in each axis, the concomitant fields have a purely quadratic spatial distribution that can be described by:

$$B_c(\mathbf{r}, t) = \frac{1}{8B_0} \mathbf{r}^T \begin{pmatrix} G_z^2(t) & 0 & -2G_x(t)G_z(t) \\ 0 & G_z^2(t) & -2G_y(t)G_z(t) \\ -2G_x(t)G_z(t) & -2G_y(t)G_z(t) & 4G_x^2(t) + 4G_y^2(t) \end{pmatrix} \mathbf{r} \quad [2.34]$$

If the field gradients are not fully symmetric around the magnetic isocenter, additional zeroth and first spatial order terms arise (85), as is most commonly the case for an asymmetric gradient coil design (86).

Constant Maxwell terms are always compensated during diffusion preparation by simple bulk displacement compensation, i.e. M_0 -nulling. For diffusion encoding waveforms which are symmetric around the echo pulse, linear and quadratic terms are compensated as well since the same gradients are experienced before and after inversion, creating the same concomitant gradient distribution. For asymmetric diffusion encoding, as investigated in this work, this is not necessarily given (3). In the case of a fully asymmetric pulse where all diffusion encoding occurs before the echo pulse, the quadratic dependence will ensure a monotonous increase in accumulated concomitant phase. The concomitant field residual phase is given by:

$$\phi_c(\mathbf{r}, t) = \gamma \int_0^{t_{diff}} B_c(\mathbf{r}, t) \operatorname{sgn}(t_{inv} - t) dt \quad [2.35]$$

In other words, ϕ_c is the additional phase accrued during traversal of the k -space trajectory modified by addition of concomitant gradient fields:

$$\mathbf{k}(\mathbf{r}) = \frac{\gamma}{2\pi} \int_0^{t_{diff}} (\mathbf{G}(t) + \nabla B_c(\mathbf{r}, t)) \operatorname{sgn}(t_{inv} - t) dt \quad [2.36]$$

In diffusion imaging, uncompensated concomitant gradients cause attenuation due to through-plane dephasing and T_2^* decay (2). The net effect is a spatially dependent signal bias, given as an attenuation factor (87):

$$AF(\mathbf{r}) = AF_{slice}(\mathbf{r}) AF_{phase}(\mathbf{r}) = |\operatorname{sinc}(d_{slice} \mathbf{n}_{slice} \cdot \mathbf{k}(\mathbf{r}))| \exp\left(-\frac{\tau}{\Delta k T_2^*} |\mathbf{n}_{phase} \cdot \mathbf{k}(\mathbf{r})|\right) \quad [2.37]$$

where d_{slice} is the slice thickness, \mathbf{n}_{slice} is a unit vector perpendicular to the imaged slice, \mathbf{n}_{phase} is the unit vector pointing in the phase encoding direction, Δt is the echo spacing and Δk is the spacing of k -space lines given by $\Delta k = R/FOV_{phase}$, where $FOV_{phase} = \mathbf{n}_{phase} \cdot \mathbf{FOV}$ is the field of view width in phase encoding direction, and R is the in-plane acceleration factor.

Asymmetric DEG waveforms can be adapted to compensate concomitant field effects. This can be performed directly, through minimizing residual phase (61), or by minimizing an intermediate *Maxwell index* (58,87). The main advantage of using the Maxwell index is rotational invariance and faster computation of the sensitivity to concomitant gradient effects in DWI. It is defined as:

$$m = \left\| \int_0^{t_{diff}} \mathbf{G}(t) \otimes \mathbf{G}(t) \operatorname{sgn}(t_{inv} - t) dt \right\|_* \quad [2.38]$$

2.4 Convex Optimization

Convex optimization is a special case of general mathematical optimization, seeking to minimize a convex function over a convex set. In its most general form, such a problem has the form:

$$\begin{aligned} & \text{minimize } f_0(\mathbf{x}) \\ & \text{subject to } f_i(\mathbf{x}) \leq b_i, \quad i = 1, \dots, m \\ & \text{with } f_i(\alpha\mathbf{x} + \beta\mathbf{x}) \leq \alpha f_i(\mathbf{x}) + \beta f_i(\mathbf{x}), \quad i = 0, \dots, m \end{aligned} \quad [2.39]$$

Problems of this kind have convex objective f_0 and constraint functions f_i satisfying the powerful property that any (local) minimum will necessarily be the global minimum of the function. A solution is given by an optimization variable $\mathbf{x} = (x_1, x_2, \dots, x_n)$ that minimizes the objective function and satisfies all constraints posed by bounds b_i .

Convex optimization has found widespread use in science and industry as an extension to linear optimization, allowing previously difficult problems to be solved in a computationally efficient manner. It is used for portfolio optimization in finance, device sizing in electronic design, and data fitting, to name a few (88). It is commonly utilized as an aid for solving a growing list of engineering and design challenges in automatic control, aerospace design, supply chain management, chemistry, and mechanical engineering. Most relevant to this work, it has also been utilized for gradient waveform optimization (3,57,60).

Its main advantages over general constrained optimization are the speed and consistent solution times with which optimal points are attained. This opens the possibility to solve larger problems and more complex models, or to develop embedded optimization solutions. Several tools for modeling and solving convex optimization problems have been created, many of which are available for free. The ease and simplicity of use of these tools have supported their adoption as a mathematical tool in science, as a more general alternative to linear or least-squares programming. Many non-convex problems can be reformulated into equivalent or approximate convex problems, resulting in broad applicability due to the comparatively lenient requirements.

Semidefinite programming is a particular area of convex optimization. A semidefinite program (SDP) is concerned with finding the optimal solution given a linear objective function constrained to a convex set given by the intersection of a cone of a semidefinite positive matrix with an affine space. These problems can be efficiently solved using interior point methods.

3 Methods

3.1 Gradient Waveform Optimization

3.1.1 Problem

The problem of optimal gradient waveform design was posed as a semidefinite programming problem maximizing the b -value for a given set of constraints and duration. A reformulation of the objective into an equivalent convex function reduces the complexity and computation requirements. Such an equivalent intermediate value is given by:

$$\beta = \int_0^{t_{diff}} k(t) dt, \quad [3.1]$$

which is a convex function (3) for $k(t)$ introduced in equation 2.16. Finding the maximum of β is equivalent to finding the maximum b -value. Due to the convexity, any local maximum of β will necessarily be the global maximum of the function, allowing for efficient solving. Finally, the objective of the optimization can be summarized in the following formulation:

$$G(t) = \arg \max_G \beta \quad [3.2]$$

For any given diffusion encoding waveform there exists a waveform with longer encoding duration t_{enc} that has a larger b -value, as can be verified through the definition given in equation 2.16. An iterative algorithm was implemented to find the waveform with shortest t_{enc} , and consequently echo time TE , that still attains the desired b -value. The upper and lower bounds for the search were appropriately initialized and solved using the Brent-Dekker method, which provides a combination between the bisection method and the secant method using the known b -values at the search space limits to provide a linear estimate of the limits for the next iteration step. The complete process used for gradient waveform optimization including the search algorithm is detailed in the flowchart in Figure 3.1.

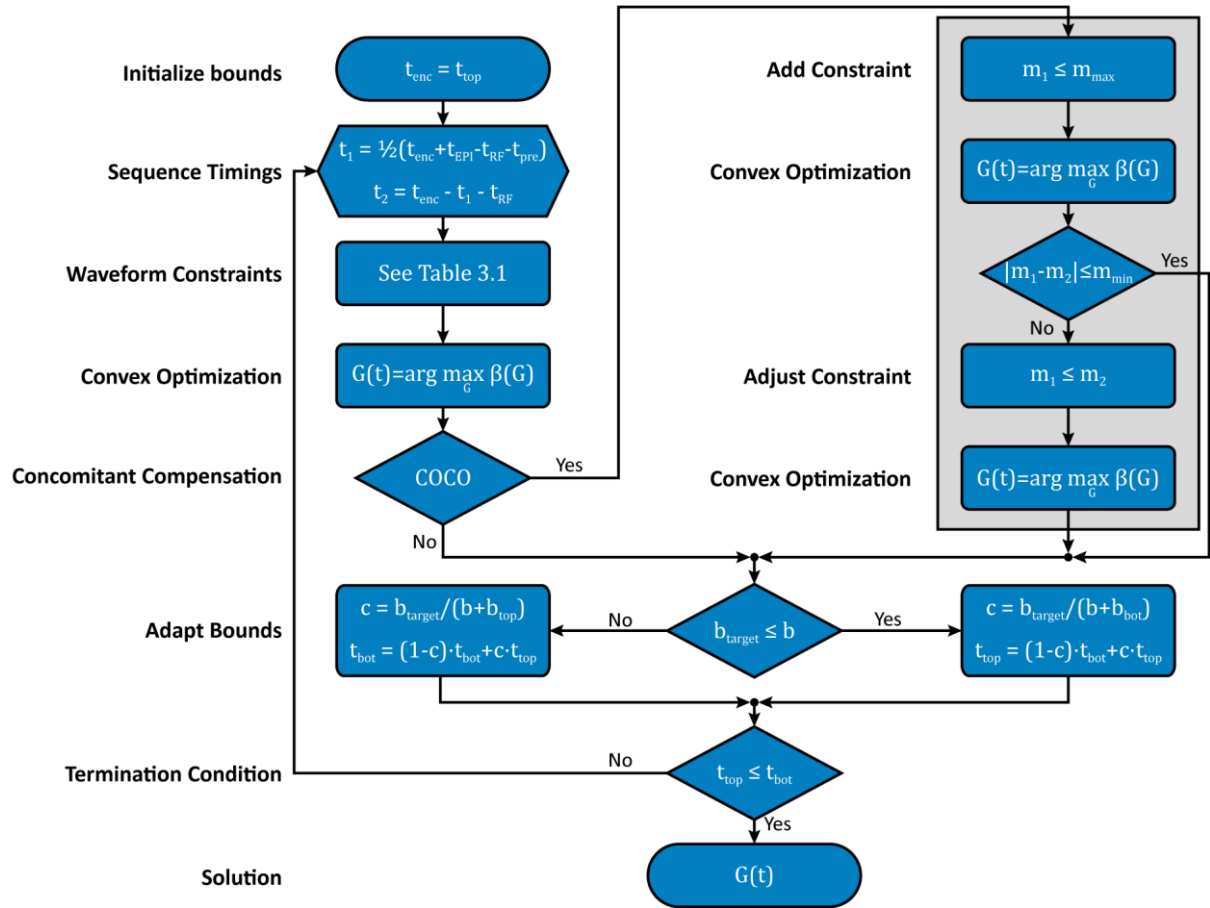


Figure 3.1: Waveform optimization process flowchart showing the adapted CODE (3) and the implemented COCO method with concomitant field compensation. Adapted from: (60)

3.1.2 Constraints

The gradient waveform design is restricted by various gradient hardware constraints, physiological constraints limiting the slew rate to avoid peripheral nerve stimulation, as well as timing constraints imposed by the implemented pulse sequence. The various constraints are summarized in the table below:

Type	Constraint	Constraint
Sequence timings	Encoding gradients are not allowed during preparation time, which includes half the 90° excitation pulse duration, as well as any rephasing lobes, navigator echoes and EPI correction lines	$G(0 \leq t \leq t_{pre}) = 0$ $t_{pre} = 2.30 \text{ ms}$
	No gradients can be switched for the duration on the 180° echo pulse	$G(t_{RF^-} \leq t \leq t_{RF^+}) = 0$ $t_{RF} = 4.62 \text{ ms}$
Hardware limits	Maximum combined gradient amplitude	$ G(t) \leq G_{max}$
	Maximum combined gradient slew rate	$ \dot{G}(t) \leq S_{max}$
Moment-nulling	Zeroth order gradient moment-nulling compensating bulk displacement	$M_0 = \int_0^{t_{enc}} G(t) dt = 0$
	First order gradient moment-nulling compensating bulk velocity (optional)	$M_1 = \int_0^{t_{enc}} t G(t) dt = 0$
	Second order gradient moment-nulling compensating bulk acceleration (optional)	$M_2 = \int_0^{t_{enc}} t^2 G(t) dt = 0$
Concomitant fields	Maxwell index limit imposed on G_1	$m_1 \leq m_{max}$

Table 3.1: Overview of constraints for the proposed optimization problem.

For simplification, the first part of the waveform, i.e. before the echo pulse, is labeled as $G_1(t) = G(0 \leq t \leq t_{RF^-})$ and the second part $G_2(t) = G(t_{RF^+} \leq t \leq t_{diff})$. The corresponding Maxwell indices are $m_1 = m(G_1)$ and $m_2 = m(G_2)$.

3.1.3 Concomitant Gradient Compensation

A complete compensation of second order concomitant gradients was implemented by expanding the above procedure. Full simulation of concomitant gradient effects in an entire volume is computationally expensive, motivating a different approach to approximate the effects on encoding performance. Such a simplification is given with the previously introduced Maxwell index. A constraint was added to the optimization (s. Table 3.1), and up to two additional optimization steps were performed in each search iteration. The first optimization step was performed without the Maxwell index constraint. The resulting waveform was used to initialize the second optimization step whereby m_1 of the waveform being optimized was constrained by m_2 of the previously obtained waveform. In certain cases, the concomitant fields were not fully compensated after the second optimization step and a third optimization was performed in the same manner. This procedure generated waveforms with $\Delta m = |m_1 - m_2| \leq 10^{-2} \mu\text{s} T^2 m^{-2}$ in all compensated waveforms. An extension to the flowchart accurately depicting the adjusted method is given in Figure 3.1. The compensation is rotationally invariant (87), hence any

projection of the optimized waveforms to physical gradient axes is possible regardless of the diffusion encoding direction and FOV orientation. The concomitant fields cause intravoxel dephasing leading to signal dropout as described in section 2.3.3. The attenuation factor was simulated for each waveform throughout the defined imaging volume according to equation 2.33 to evaluate concomitant gradient compensation for a fixed encoding direction. The attenuation at the edge of the imaging volume was compared to determine the worst-case signal bias introduced. The parameters used are given below:

Parameter	d_{slice}	\mathbf{n}_{slice}	\mathbf{n}_{phase}	T_2^*	R	Δk	τ	FOV	$\mathbf{n}_{gradient}$
Value	5 mm	[0, 0, 1]	[0, 1, 0]	25 ms	1	4 m ⁻¹	0.242 ms	25 × 25 × 15 cm	[1, 1, 1]

Table 3.2: Overview of concomitant attenuation simulation parameters.

3.1.4 Waveform Simulation

A custom framework was implemented for MATLAB (MathWorks, Natick, Massachusetts). Gradient waveform optimization was performed using the YALMIP optimization toolbox (89) to model the problem and ILOG CPLEX Optimization Studio (IBM, Armonk, New York) for solving. A discretization timestep $dt = 100\mu s$ was chosen for numerical modelling of the physical gradient waveforms. The resulting waveforms were upsampled to $dt' = 10\mu s$ for implementation on the Siemens software platform using a piecewise cubic interpolation method available in MATLAB. A database of optimized waveforms was generated from a range of values for each parameter: $t_{EPI} = 12 - 32\text{ ms}$; $b = 100 - 1000\text{ s/mm}^2$; $G_{max} = 40 - 300\text{ mT/m}$; $S_{max} = 50 - 200\text{ T/m/s}$. For each parameter combination a set of three waveforms were generated:

- a) symmetric diffusion encoding waveforms MONO/BIPOLAR/MOCO, respectively for $M_0/M_1/M_2$ -nulled waveforms;
- b) adapted Convex Optimized Diffusion Encoding (3) waveforms CODE- $M_0/M_1/M_2$;
- c) the proposed asymmetric waveforms with concomitant compensation COCO- $M_0/M_1/M_2$.

For the longest investigated waveforms, the optimization of a single gradient waveform took $8.70 - 40.32\text{ s}$ for CG-compensated waveforms and $1.83 - 10.68\text{ s}$ in the non-compensated case on a notebook PC with a dual-core Intel i7-7500U CPU clocked at 2.70GHz accelerated using built-in parallel computing capabilities of the CPLEX solver. The computing duration depends on desired b -value, moment-nulling and system constraints. This database was used for all subsequent analyses and measurements. Generated waveforms for $b = 1000\text{s/mm}^2$, $G_{max} = 150\text{ mT/m}$, $S_{max} = 62.5\text{T/m/s}$ and $t_{EPI} = 16\text{ ms}$ are given in Figure 3.2.

The results of the simulation were evaluated to compare the different waveform optimization techniques. A comparison of echo time TE was performed and the absolute and relative reduction of TE was calculated between symmetric and both asymmetric waveform types. The gradient moment evolution was evaluated for each simulated waveform and compared. Large peaks in the gradient accrual during the encoding can affect the motion-robustness of a sequence negatively if higher-order motion components are present. A similar argument can be made regarding peaks in the residual phase of concomitant field and eddy-current effects. The gradient moment maxima, final values and standard deviation of each moment order, as well as maximal and final values for concomitant and eddy-current residual phase were compared to evaluate susceptibility to motion-related artifacts.

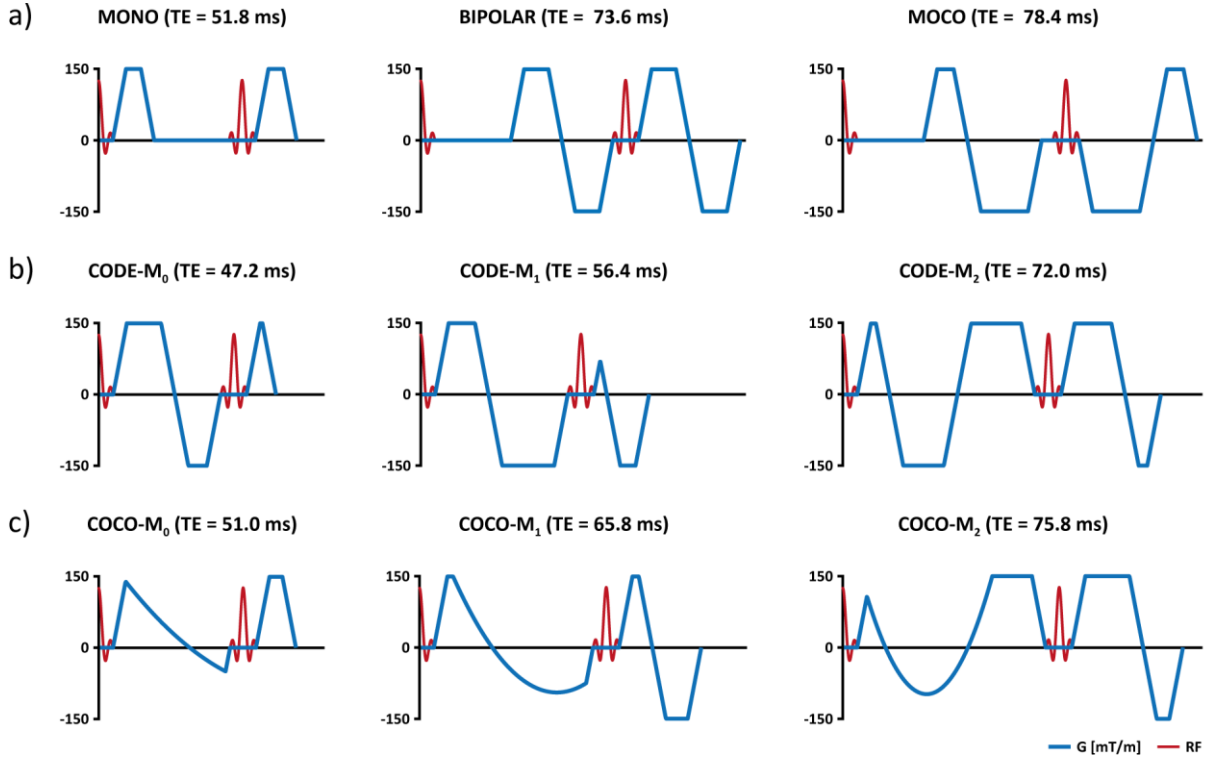


Figure 3.2: Comparison of optimized waveforms: a) symmetric designs (MONO, BIPOLAR, MOCO); b) CODE- $M_0/M_1/M_2$ waveforms; c) COCO- $M_0/M_1/M_2$ waveforms.

3.2 Imaging Experiments

All imaging experiments were carried out on a Magnetom Skyra Connectom MRI system (Siemens, Erlangen, Germany) described in section 1.2, with custom spin echo pulse sequences implementing the optimized waveforms using a single-shot EPI readout (9). The experiments were carried out on an aqueous diffusion phantom, an *in vivo* human brain and an *in vivo* pig heart. The acquisition procedures for all three datasets are presented below, whereas detailed analysis of the resulting images can be found in section 4.2.

No ghosting or further post-processing corrections were applied. The background was masked in the figures presented in the presented results. This was achieved through a simple thresholding of the raw signal amplitude against the mean signal intensity for a given image.

3.2.1 Phantom Imaging

A water-based imaging phantom (Siemens, Erlangen, Germany) was imaged with a 64-channel custom head/neck array coil (90). A single axial slice located at an offset $d_z = 40\text{ mm}$ from the magnetic isocenter was imaged with an in-plane field of view of $FOV_{xy} = 20 \times 20\text{ cm}^2$ at a resolution of $[\Delta x, \Delta y, \Delta z] = 1.82 \times 1.82 \times 10\text{ mm}^3$. The resulting matrix of 110×110 pixels was acquired with a receiver bandwidth of $2165\text{ Hz}/\text{px}$. Waveforms optimized with gradient slew rate constrained to $S_{max} = 50\text{ T}/\text{m}/\text{s}$, and amplitude constrained to $G_{max} = 80\text{ mT}/\text{m}$ and $G_{max} = 150\text{ mT}/\text{m}$ were used. Acquisitions were made with the full set of generated waveforms (MONO/BIPOLAR/MOCO, CODE- $M_0/M_1/M_2$ and COCO- $M_0/M_1/M_2$). All acquisitions had $TE = 90\text{ ms}$ and were performed first without diffusion encoding (b_0 -map) then with diffusion encoding in each of the three principal scanner axes $[x, y, z]$. Waveforms that were optimized to

match a shorter TE had an additional dead-time after excitation and before the start of the diffusion encoding to match the desired echo time. This was done to evaluate concomitant field compensation under the same conditions, i.e. with same T_2 -weighting and roughly equal SNR.

The resulting images were evaluated and compared according to calculated metrics. Diffusion in the phantom is expected to be homogeneous under thermal equilibrium, so spatial variations are largely attributable to gradient effects. Histograms of the acquired images were generated for comparison between evaluated encoding methods. The coefficient of variation over the whole phantom region was calculated for each image to quantify spatial distortions of the encoding methods.

3.2.2 *In Vivo* Brain Imaging

A healthy volunteer was scanned using a 12-channel head array coil (Siemens, Erlangen, Germany) within a scan protocol subject to MGH Institutional Review Board approval. A single axial slice passing through the cerebrum was imaged at resolution $[\Delta x, \Delta y, \Delta z] = 2.18 \times 2.18 \times 5 \text{ mm}^3$ with $FOV_{xy} = 27.9 \times 27.9 \text{ cm}^2$, for a matrix size 128×128 pixels and receiver bandwidth $2440 \text{ Hz}/\text{px}$. Diffusion weighted images with varying b -values were acquired using waveforms optimized for specific gradient hardware constraints, as summarized in Table 3.3. The acquisition was performed both at isocenter ($d_z = 0 \text{ mm}$) and repeated after shifting the patient table by 40 mm along the bore to evaluate concomitant field effects in z direction. Due to comparatively small motion effects in brain imaging, no bulk velocity of acceleration compensation was used; all acquisitions were made with M_0 -nulled waveforms (MONO, CODE- M_0 or COCO- M_0).

For each gradient strength and encoding waveform type an image was acquired with diffusion sensitizing gradients switched in the read, phase and slice directions $[x, y, z]$ and once without diffusion encoding. The cerebral tissue was delineated manually and used to mask the background. Four regions of interest were drawn in representative areas and statistical analysis was performed over ADC maps calculated from acquired images for all waveform types.

Scan	b	G_{max}	S_{max}	TE	d_z
1	500 s/mm^2	80 mT/m	50 T/m/s	72 ms	0 mm
2	500 s/mm^2	150 mT/m	50 T/m/s	72 ms	0 mm
3	500 s/mm^2	150 mT/m	50 T/m/s	72 ms	40 mm
4	400 s/mm^2	250 mT/m	42 T/m/s	78 ms	40 mm
5	350 s/mm^2	270 mT/m	45 T/m/s	78 ms	40 mm

Table 3.3: *In vivo* brain imaging parameter combinations. Five separate scans with different parameter combinations were acquired with different target b -values, maximum gradient strengths, maximum slew rate limits, echo times, and offset in z -direction.

3.2.3 *In Vivo* Heart Imaging

With approval of the Institutional Animal Care and Use Committee of the Massachusetts General Hospital, an adult pig was anesthetized and imaged *in vivo* using an 8-channel spine matrix coil and 12-channel phased array coil (both Siemens, Erlangen, Germany). A three-dimensional acquisition of the heart was performed, capturing the full heart volume within 12 parallel axial-

sagittal slices, providing a short-axis view through the myocardium with a slice thickness of 8 mm. The in-slice resolution was $2.6 \times 2.6 \text{ mm}^2$, covering a transversal field of view of $12 \times 26 \text{ cm}^2$ on an imaging matrix consisting of $46 \times 100 \text{ px}$. Each slice was acquired with diffusion-preparation at $b = 500 \text{ s/mm}^2$ in six non-colinear directions: [1,0,1], [-1,0,1], [1,1,0], [1,-1,0], [0,1,1], [0,1,-1]. Hereby the directions are specified in relation to the imaging axes corresponding to frequency, phase, and slice (long axis) directions, respectively.

Optimized MOCO, CODE- M_2 and COCO- M_2 waveforms constrained to $G_{max} = 150 \text{ mT/m}$ and $S_{max} = 50 \text{ mT/m}$ were used nulling zeroth, first and second order gradient moments in order to reduce motion effects on imaging. The acquisitions were ECG-gated to synchronize encoding and data readout with the diastole where the least motion is expected in the cardiac cycle. The echo time of the sequence was $TE = 68 \text{ ms}$, the readout duration was defined with $t_{EPI} = 16 \text{ ms}$, and a trigger-dependent minimal repetition time was chosen at $TR = 230 \text{ ms}$. The acquired diffusion-weighted images were reconstructed into a diffusion tensor using custom software based on DIPY (www.dipy.org) with a procedure as described in (70). The orientation of the principal diffusion directions was utilized to calculate the helix angle in a cross-section of the myocardium. A description of the helix angle (HA) calculation is given in Figure 3.3. The evaluated helix angles obtained using both CODE- M_2 and COCO- M_2 waveforms were compared against the ground truth MOCO waveforms to evaluate diffusion encoding.

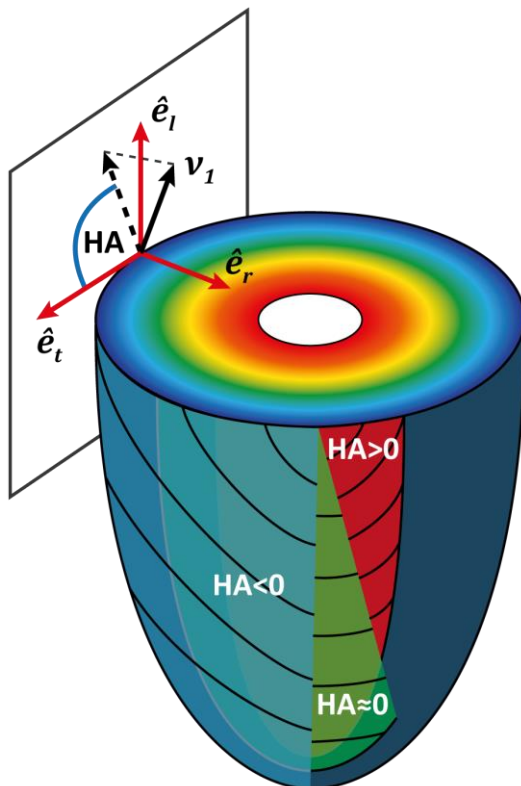


Figure 3.3: Illustration of cardiac helix angle. To define this angle, we construct a local coordinate system in the point of interest within the myocardium with radial axis \hat{e}_r coinciding with the short axis of the heart, longitudinal axis \hat{e}_l in the direction of the long axis of the heart and a tangential axis \hat{e}_t . The fiber orientation given by the principal diffusion direction ν_1 , is projected onto the tangential plane facing in the radial direction. HA is defined as the angle between the projection and the tangent on the short axis slice circumference given by \hat{e}_t . For normal myocardium, the helix angle is positive in the endocardium and negative in the epicardium. Adapted from: (91,92)

3.3 Error and Noise Quantification

Errors in diffusion measurements propagate and have an impact on the final diffusion metrics as described in section 2.2. For evaluation of the implemented waveforms, root-mean-square errors (RMSE) comparing ground truth data to method results were calculated, and the signal-to-noise ratio (SNR) of several regions of interest (ROI) was determined to quantify the quality of diffusion encoding based on signal loss from undesirable effects.

The RMSE is defined as the quadratic mean of the difference in value of predicted and observed values. It is utilized to quantify the deviation of one sample population to another. In MRI this is frequently used to compare ground truth and equivalent measured values, i.e. the difference of signal intensity values on a per-pixel basis. It is defined as:

$$RMSE(\mathbf{x}, \mathbf{y}) = \sqrt{\frac{(x_1 - y_1)^2 + (x_2 - y_2)^2 + \dots + (x_n - y_n)^2}{N}} = \sqrt{\frac{\sum_{i=1}^N (x_i - y_i)^2}{N}} \quad [3.3]$$

The SNR is given by the ratio of mean useful signal (\bar{S}_{use}) and background noise standard deviation (σ_{noise}^2). ROIs were drawn in the object image area to define the useful signal, and in regions with background air to estimate the noise level. The factor (~ 0.655) in the equation below is due to the Rician distribution of noise in air (93). The SNR was utilized to evaluate if diffusion encoding was negatively impacted by gradient effects causing signal loss in target areas. Comparisons were drawn between implemented methods based on obtained values:

$$SNR = \sqrt{2 - \frac{\pi}{2}} \frac{\mu_{signal}}{\sigma_{noise}} \quad [3.4]$$

To quantify spatially distributed measurement bias in homogeneous regions, the coefficient of variation (COV) is a useful metric for comparisons. This is given as the ratio of the standard deviation and mean of signal values within a region of interest:

$$COV = \frac{\sigma(ROI)}{|\mu(ROI)|} \quad [3.5]$$

4 Results and Evaluation

The results are presented in two parts. The first section compares symmetric and optimized asymmetric waveforms regarding basic values, echo time, motion sensitivity, and concomitant field attenuation. In the second part of the chapter, results from the imaging experiments are shown and evaluated based on previously established metrics. The assessment of the method focuses on the effects of the concomitant field effects on final diffusion metrics.

4.1 Waveform Simulation

4.1.1 Echo Time Reduction

For a given parameter set of moment nulling order, b -value, maximum gradient amplitude, maximum gradient slew rate and readout duration, the waveforms were compared for minimum attainable echo time. Within the simulated parameter range, the optimized COCO gradient waveforms were found to have a reduced TE compared to the comparable symmetric gradient waveforms with same encoding parameters in all cases. For M_0 -nulled waveforms (MONO vs. COCO- M_0) the reduction in TE was modest, whereas for higher order gradient moment nulling the TE reduction was more significant. Compared to the adapted CODE waveforms without concomitant gradient nulling, the COCO waveforms were found in all cases to have an increased TE. This was due to the additional Maxwell index constraint which caused a quadratically shaped slew de-rating in the first section of the encoding prior to the spin inversion. A summary of achieved TE reduction against the symmetric DEG waveforms over the full parameter set is summarized in Table 4.1. A comparison of the three methods over a subset of parameters is given in Figure 4.1, showing the TE for a specified G_{max} , S_{max} and t_{EPI} over the full range of b -values.

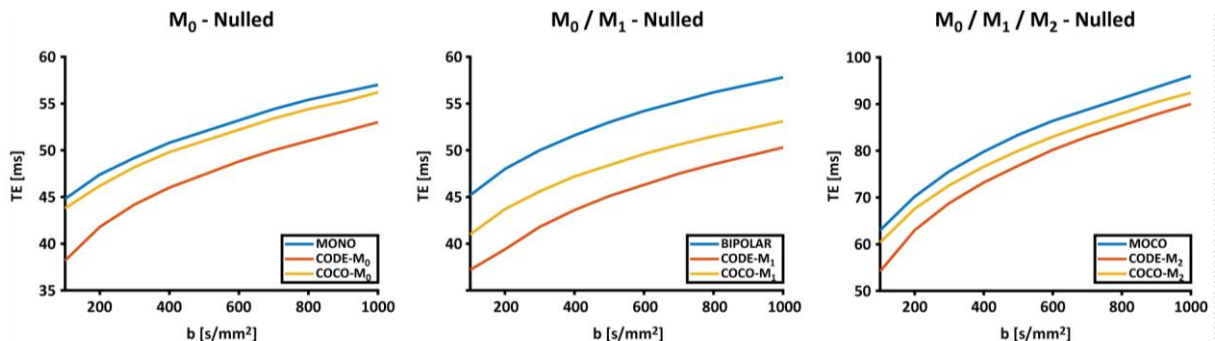


Figure 4.1: Minimum echo time achieved for a range of b -values from $100 - 1000 \text{ s/mm}^2$ and readout duration till center of echo $t_{EPI} = 16 \text{ ms}$. The waveforms were restricted to maximum combined amplitude of $G_{max} = 80 \text{ mT/m}$ and slew rate of $S_{max} = 100 \text{ T/ms}$.

Type	$M_0 = 0$	$M_0 = M_1 = 0$	$M_0 = M_1 = M_2 = 0$
COCO	-0.6 – 2.8 ms	5.0 – 19.0 ms	1.0 – 9.2 ms
CODE	1.6 – 16.2 ms	10.0 – 33.0 ms	3.2 – 30.4 ms
COCO	-1.02 – 3.54 %	7.31 – 17.08 %	1.10 – 9.73 %
CODE	2.42 – 20.24 %	9.62 – 32.22 %	3.09 – 27.94 %

Table 4.1: TE reduction of asymmetric relative to symmetric waveforms. Across all compared parameters described in 3.1.4, excluding parameters where the resulting symmetric waveform was de-rated, the adapted CODE waveforms consistently outperformed both symmetric and COCO waveforms. Of the methods with CG-nulling, COCO resulted in shorter waveforms than symmetric sequences for all cases, with exception of the M_0 -nulled with a short readout ($t_{EPI} = 12$ ms).

Generally, the TE reduction was greater for larger b -values and longer t_{EPI} for both COCO and CODE. An overview of the achieved reduction comparing MONO, BIPOLAR and MOCO with corresponding CODE and COCO sequences is given in Figure 4.2. The reduction was greatest for M_1 -nulled and lowest for M_0 -nulled waveforms. This can be explained by the design of BIPOLAR waveforms, which do not include a mixing time before the echo pulse, whereas MONO and MOCO waveforms do. For long readouts, where the available encoding time is extended due to echo timing considerations, MONO sequences utilize the additional idle time to increase diffusion sensitizing by including it in t_{mix} . Consequently, CODE- M_0 and COCO- M_0 show only slight improvements over MONO. MOCO waveforms do not include the full idle time in t_{mix} due to moment nulling requirements. CODE waveforms suffer from long idle times for small b -values or long t_{EPI} , whereas COCO utilizes all available time for CG reduction.

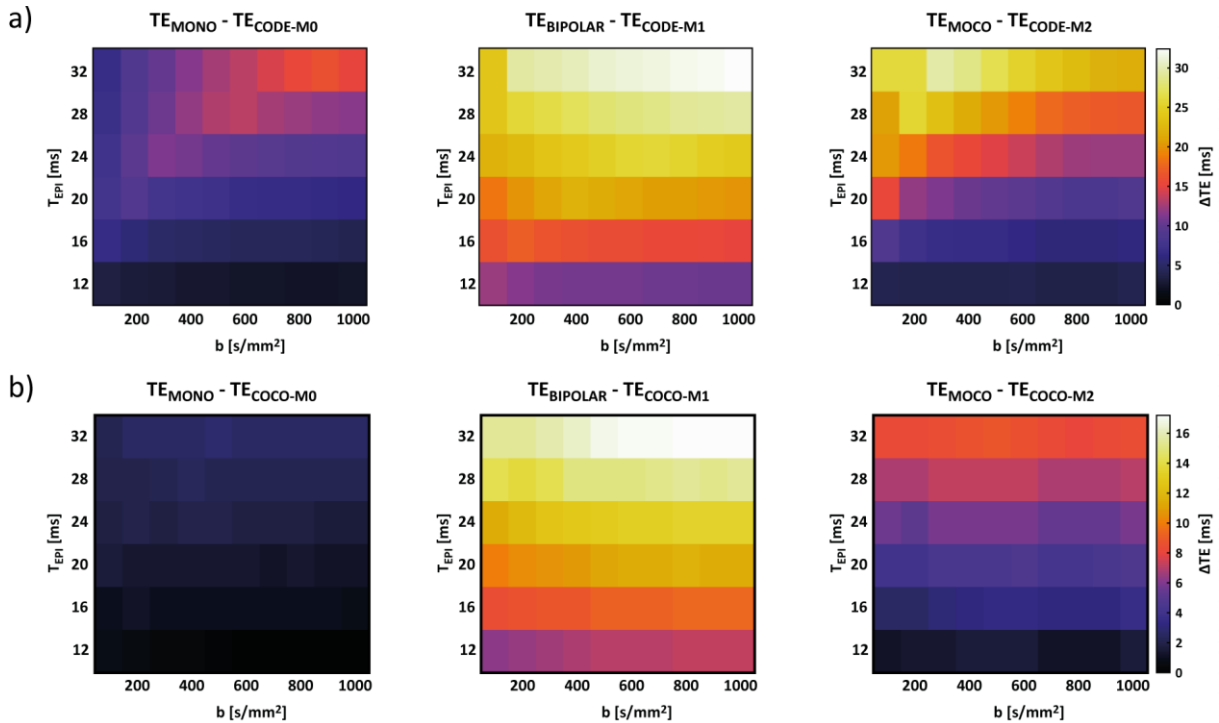


Figure 4.2: Comparison of echo time reduction over the full range of optimized t_{EPI} values in the range from 12 – 32 ms in 4 ms steps, and b -values from 100 – 1000 s/mm^2 in increments of 100 s/mm^2 . All values are given for waveforms with $G_{max} = 80$ mT/m and $S_{max} = 100$ $T/m/s$. For both, adapted CODE and COCO waveforms, the reduction is greater for long readouts.

4.1.2 Concomitant Gradient Compensation

The concomitant gradients cause an additional phase accumulation $\phi_c(t)$. The phase shift is generally larger for points in the imaging volume that are at a larger distance from the magnetic isocenter. The concomitant gradient (CG) phase was calculated for simulated waveforms with $t_{EPI} = 16 \text{ ms}$ and $S_{max} = 100 \text{ T/m/s}$ in the worst-case pixel of the imaging volume defined by the FOV. Figure 4.3 a) – c) show the maximum attained phase, for each of the simulated waveform types and optimized with increasing gradient amplitude constraints. The maximum phase is reached during the refocusing pulse after the end of the first gradient waveform segment. After the inversion, the symmetric and asymmetric COCO waveforms fully refocus ϕ_c at the end of the diffusion encoding, whereas the CODE waveforms leave a residual phase which impacts the diffusion signal readout. Figure 4.3 d) shows the residual phase of CODE waveforms at time t_{diff} . Higher G_{max} limits and larger b -values generally lead to greater phase accumulation.

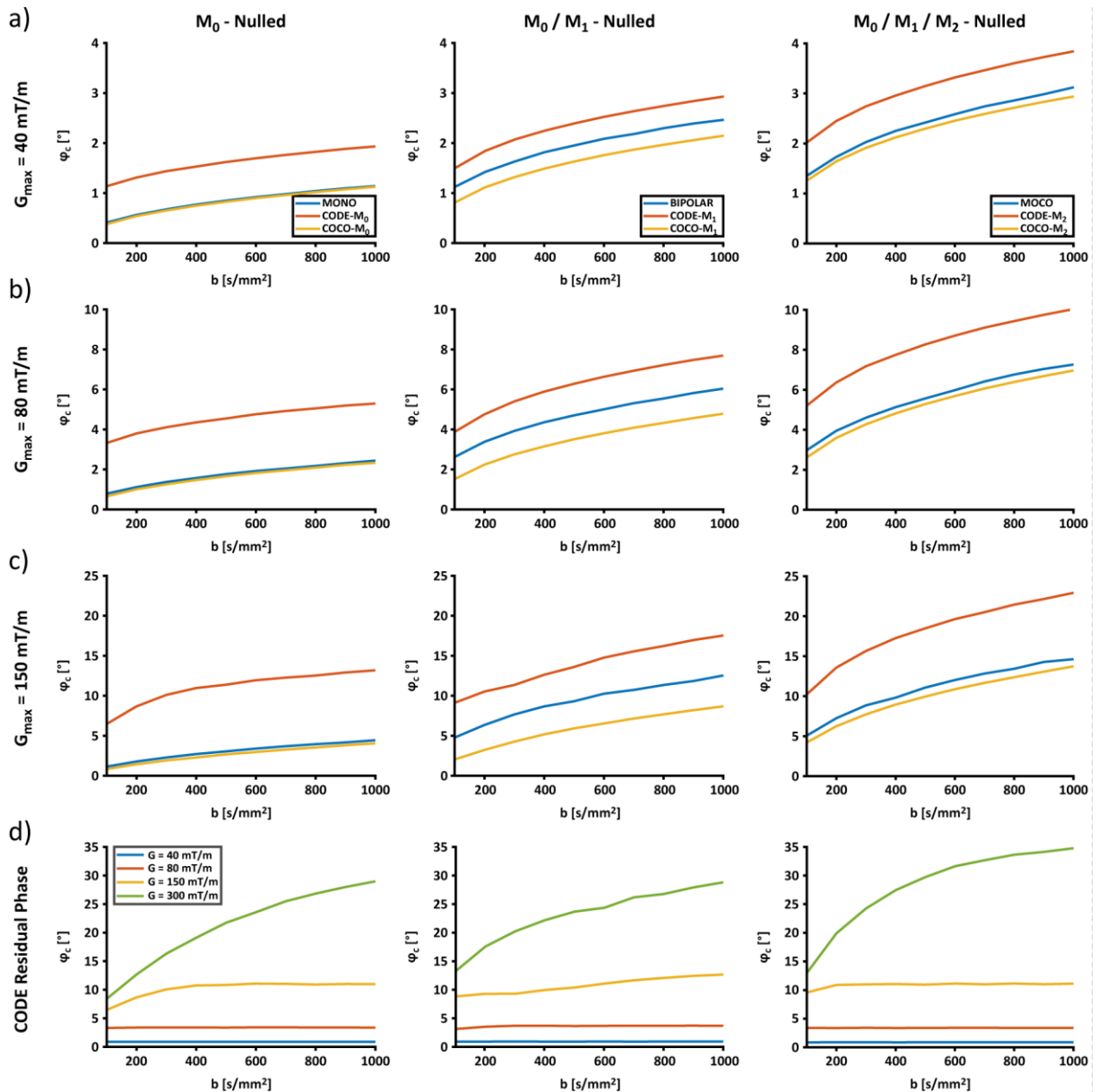


Figure 4.3: Concomitant gradient phase accumulation during encoding. a) – c) show the maximum phase for all waveform types; d) shows the residual phase of CODE waveforms for various b -values. All values are simulated for the worst-case voxel according to parameters given in Table 3.2.

Non-compensated CG phase shifts lead to signal dropout. This bias is in relation to the accumulated phase as well as imaging parameters and is described by equation 2.37

$$AF(\mathbf{r}) = AF_{slice}(\mathbf{r}) AF_{phase}(\mathbf{r}) = |\text{sinc}(d_{slice} \mathbf{n}_{slice} \cdot \mathbf{k}(\mathbf{r}))| \exp\left(-\frac{\tau}{\Delta k T_2^*} |\mathbf{n}_{phase} \cdot \mathbf{k}(\mathbf{r})|\right) \quad [2.37]$$

. For the generated waveforms, the physical distribution of signal attenuation in a given volume can be calculated and visualized. Figure 4.4 below shows the evaluation of attenuation in cross-sectional slices of the simulation volume for a) the CODE- M_0 waveform, and b) the COCO- M_0 waveform optimized for $b = 1000 \text{ s/mm}^2$, $G_{max} = 80 \text{ mT/m}$, $S_{max} = 100 \text{ T/m/s}$ and $t_{EPI} = 16 \text{ ms}$. These waveforms had an echo time of $TE_{CODE-M_0} = 53.0 \text{ ms}$ and $TE_{COCO-M_0} = 56.1 \text{ ms}$ for the chosen parameters. The relative signal is given as a percentage of the signal without any attenuation. For the CODE encoding, the signal attenuation is greater in the edges of the FOV, whereby there is an effect in all axes for the chosen diffusion encoding direction [1,1,1] given by the frequency, phase and slice direction respectively. The diffusion encoding using the optimized COCO waveform shows no significant CG effects in any voxel. The worst-case voxel, marked in the figure below, shows an increasing signal bias for increasing diffusion-sensitivity in the CODE case, whereas the concomitant compensated case matches the expected signal attenuation due to the diffusion encoding as simulated for a homogenous diffusion coefficient of $D = 1 \text{ mm}^2/\text{s}$, showing no additional signal loss due to CG effects.

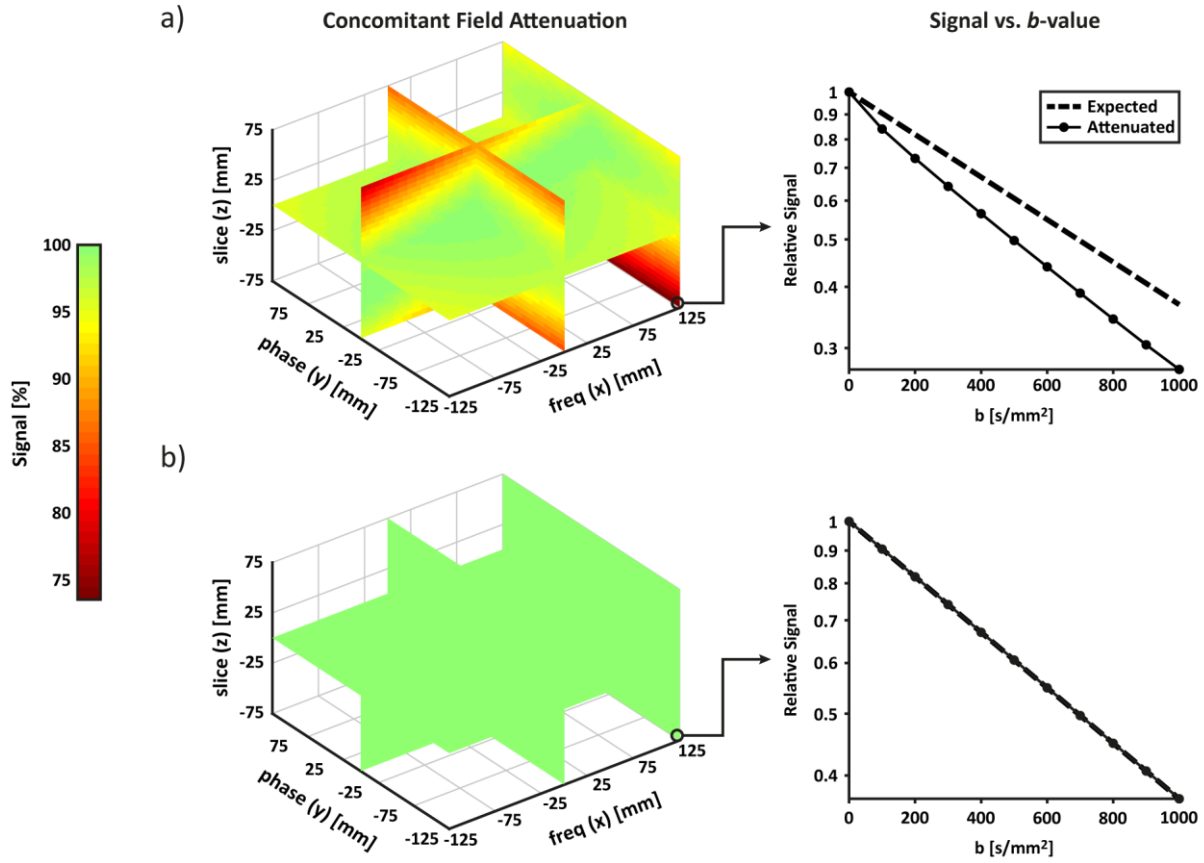


Figure 4.4: Simulation of concomitant field attenuation in a simulated imaging volume. The examples show two equivalent DEG waveforms: a) CODE- M_0 and b) COCO- M_0 . The signal dropout caused by concomitant gradient residual phase is evident for the non-compensated CODE waveforms, whereas COCO waveforms exactly match expected signal in even the worst-case voxel. The increase in encoding time is modest at $\Delta TE = 3.1 \text{ ms}$ or 5.85 %, whereby the maximum signal loss over 25.4 % is significant for large FOV or for imaging areas at a large distance from the magnetic isocenter. Adapted from: (87)

As the signal attenuation is caused by intravoxel effects, the influence of concomitant gradient fields on the diffusion encoding can be diminished by increasing intravoxel phase coherence. Besides compensating concomitant fields, intravoxel dephasing can be reduced by decreasing voxel size, i.e. when imaging at higher resolutions. The components of the signal attenuation are attributed either to *through-plane* effects which depend on slice thickness d_z , or *in-plane* effects (2) dependent on Δk , the acquisition k -space sampling rate in the phase encoding direction. The signal attenuation of the CODE- M_0 waveform shown in Figure 4.4 is separated into individual components and is displayed in Figure 4.5. The attenuation components are simulated for the same resolution as above and for an increased resolution achieved by doubling Δk and cutting d_z in half. For the chosen parameters, the through-plane effects are more significant than in-plane attenuation effects. They are also reduced to a larger degree through increasing resolution. However, the slice thickness is typically selected to obtain a viable SNR value and further reductions are rarely possible without a proportional reduction in available signal. The reduction in concomitant gradient attenuation provided through increased resolution in the phase encoding direction alone is not significant enough to mitigate unwanted effects. This leads to the conclusion that concomitant compensation is required for cases where it leads to significant signal bias and cannot be compensated through a smaller voxel size. The shorter CODE waveforms offer reduced TE and consequently a potentially higher SNR, but this is unlikely to allow a significant reduction in slice thickness to significantly reduce CG effects.

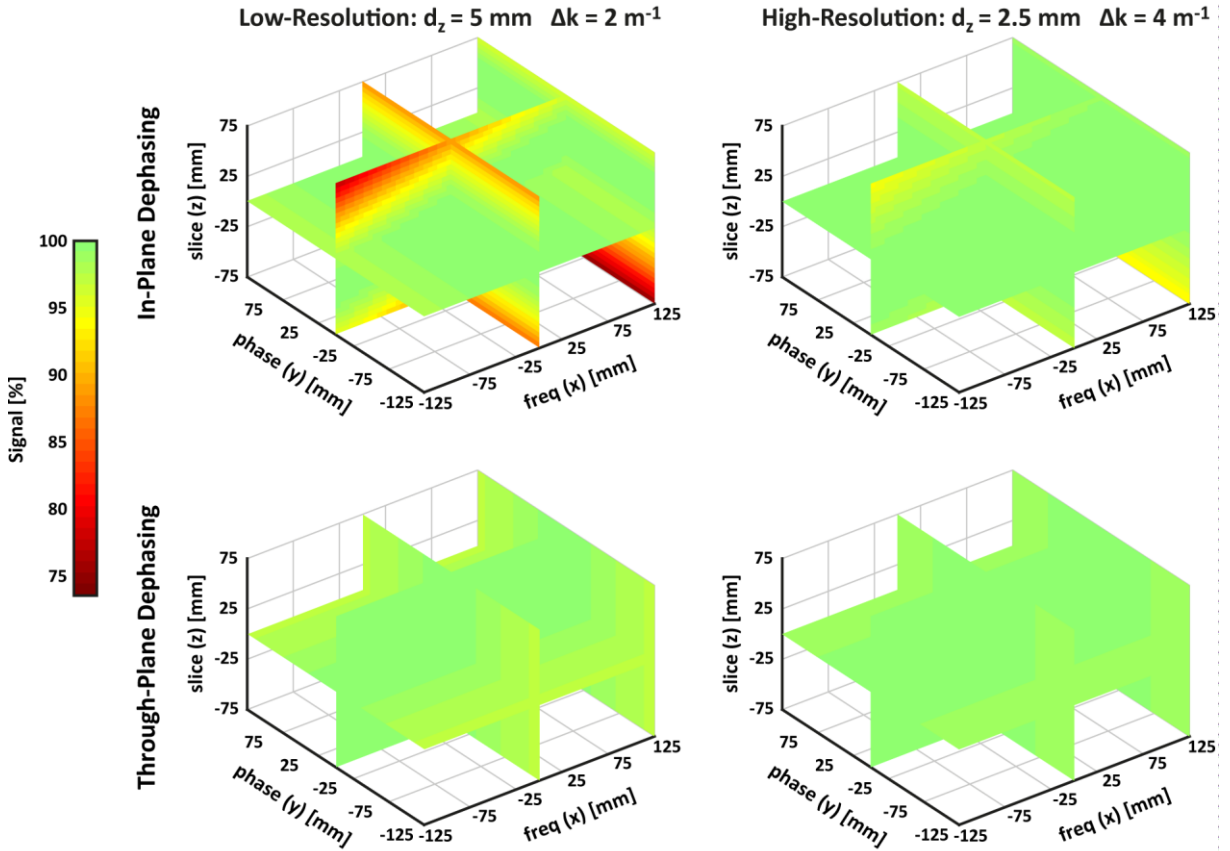


Figure 4.5: Effect of resolution on concomitant fields. The signal attenuation is separated into through-plane (top row) and in-plane (bottom row) effects, given by AF_{slice} and AF_{phase} respectively. The CG attenuation was simulated for the same CODE- M_0 waveform as shown in Figure 4.4, but evaluated at two resolutions. The first column was evaluated using $d_z = 5 \text{ mm}$ and $\Delta k = 2 \text{ m}^{-1}$, whereas the left column used $d_z = 2.5 \text{ mm}$ and $\Delta k = 4 \text{ m}^{-1}$.

4.1.3 Gradient Moment Evolution

The gradient moments cause a phase shift proportional to the corresponding order of bulk motion if they are not compensated at the start of the readout. Furthermore, the evolution during the encoding allows drawing conclusions about higher-order motion sensitivity. It is beneficial to show a shallow moment evolution with values close to zero during and at the end of encoding. Figure 4.6 compares the evolution of zeroth, first and second order gradient moments of all investigated waveform types. COCO waveforms show slightly improved M_0 moment evolution due to the softer gradient slewing in the first gradient segment $G_1(t)$, whereas CODE waveforms show better behavior for higher order due to the overall shorter encoding duration.

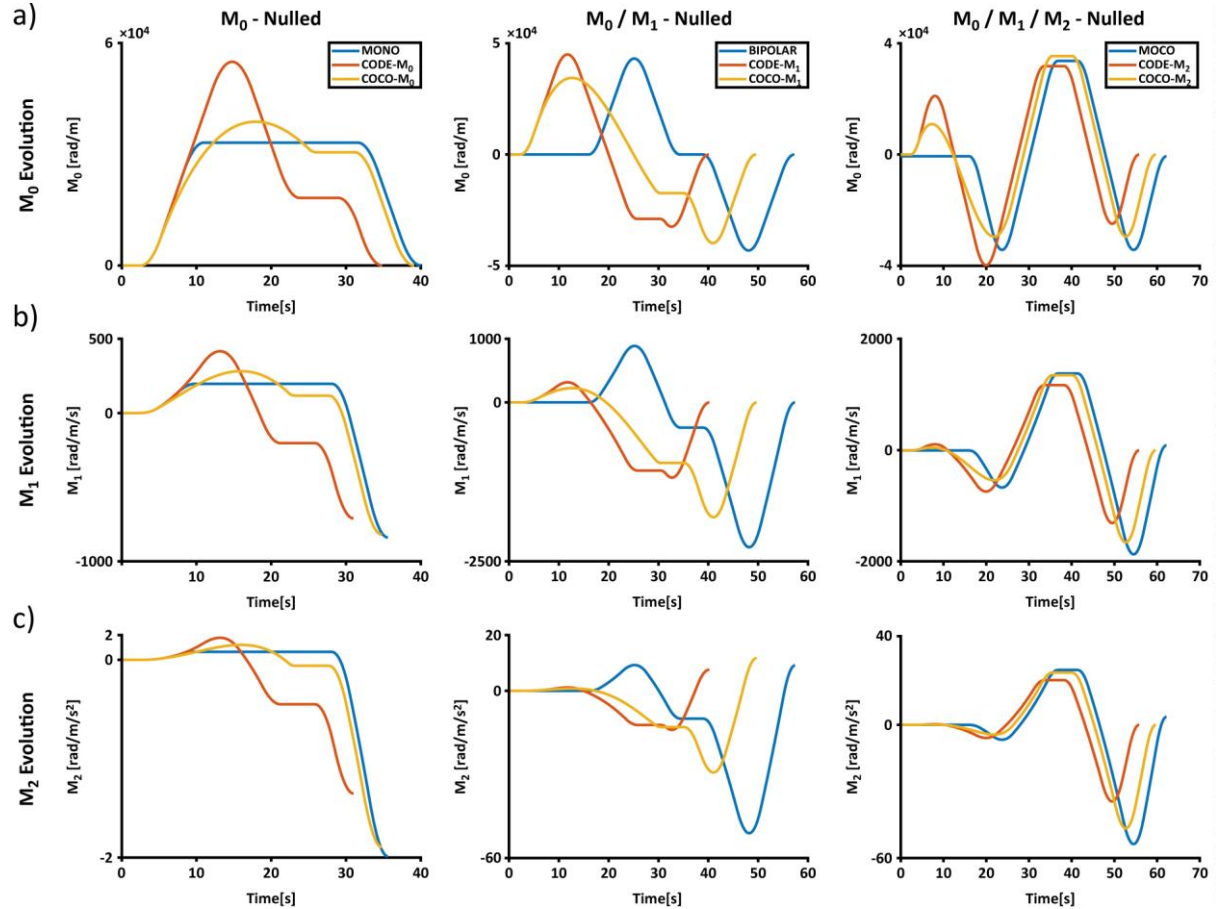


Figure 4.6: Evolution of gradient moments during diffusion encoding. The evolution of a) zeroth, b) first, and c) second order are displayed for waveforms optimized using $b = 1000 \text{ s/mm}^2$, $G_{max} = 150 \text{ mT/m}$, $S_{max} = 62.5 \text{ T/m/s}$ and $t_{EPI} = 16 \text{ ms}$.

4.2 Evaluation of Imaging Experiments

4.2.1 Phantom Acquisitions

Diffusion-weighted images were obtained from a water phantom and analyzed in order to compare the implemented methods. At $G_{max} = 80 \text{ mT/m}$, the resulting ADC maps from CODE- M_1 waveforms show a mean diffusivity value of $MD = 2.83 \text{ mm}^2/\text{s}$, a 21% overestimation of the expected diffusivity values ($ADC_{water} = 2.3 \times 10^{-3} \text{ mm}^2/\text{s}$). The overestimation is due to signal attenuation in the diffusion encoded acquisition compared to the reference signal with $b_0 = 0 \text{ s/mm}^2$ used for calculation of the ADC value. It is largely caused by through-plane intravoxel dephasing of concomitant gradient fields and are corrected in the results acquired with COCO- M_1 encoding. The acquisition results are shown along with the corresponding histograms in Figure 4.7, hereby the background noise was removed using a simple thresholding approach on the raw magnitude images. The differences are particularly evident in the results with diffusion encoding in the x and y directions. The effect shows a spatial dependence, being stronger in areas further away from the center. Eddy-current distortions are not corrected and are evident at the upper edge of the acquisition and strongly effect the calculated COV values.

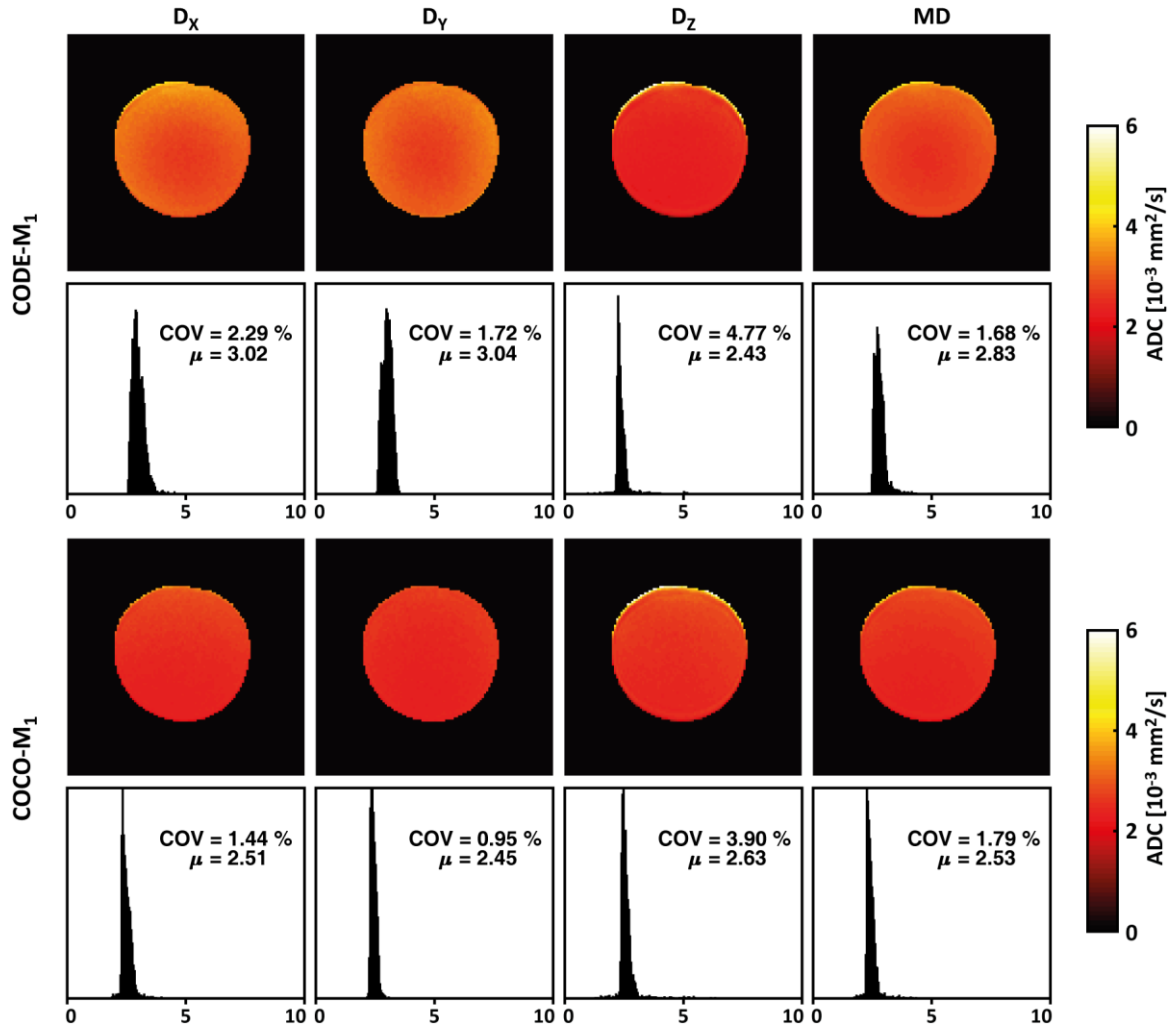


Figure 4.7: ADC maps from phantom experiments. The data was acquired using CODE- M_1 and COCO- M_1 waveforms optimized using $b = 500 \text{ s/mm}^2$, $G_{max} = 80 \text{ mT/m}$, $S_{max} = 50 \text{ T/m/s}$ and $t_{EPI} = 16 \text{ ms}$. The CODE- M_1 results shows an overestimation which disappears for COCO- M_1 .

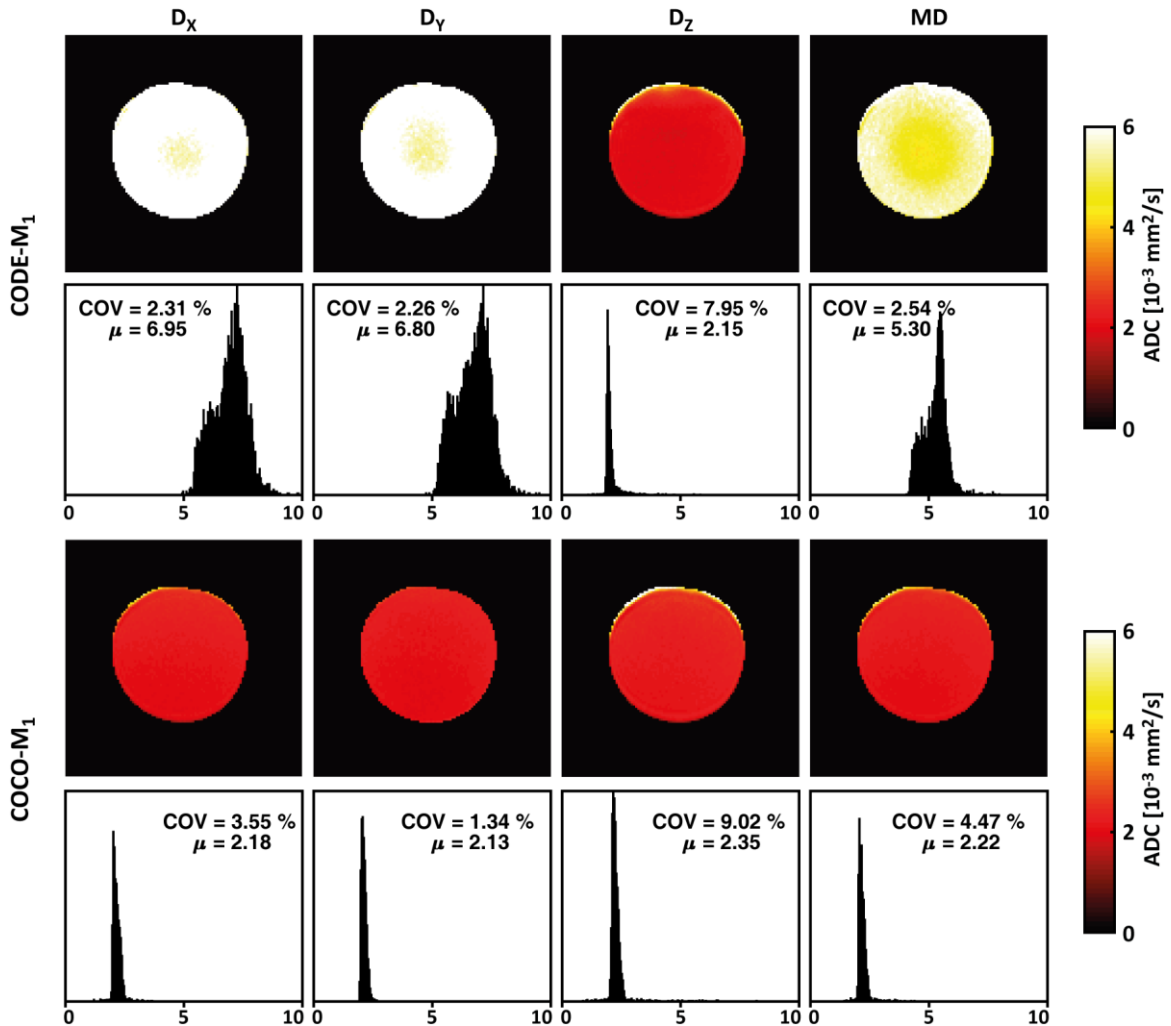


Figure 4.8: ADC maps from phantom experiments at high gradient amplitudes. The same parameters were used for waveform optimization as for Figure 4.7, but for with a higher gradient amplitude limit of $G_{max} = 150 \text{ mT/m}$. The waveform implementation on the MR scanner further exaggerates the CG distortions in the CODE- M_1 case which are again fully corrected for in the COCO- M_1 maps. For comparison, the expected minimal echo times are: $TE_{BIPOLAR} = 73.6 \text{ ms}$, $TE_{CODE-M_1} = 56.4 \text{ ms}$ and $TE_{COCO-M_1} = 65.8 \text{ ms}$. The echo time used in this case was matched with additional idle time to $TE = 90 \text{ ms}$ in all phantom acquisitions.

4.2.2 In Vivo Brain DWI

Four elliptical regions of interest were defined in the brain images and numbered ROI 1 - 4. The background region (ROI 4) was used to determine the noise floor of the acquisitions based on the raw magnitude images obtained using each method. The noise level was used to calculate the SNR of the remaining regions and the whole cerebrum as defined by a manually drawn mask. The SNR of the regions and an analysis of ADC values for the acquisition of scan 2, described in Table 3.3, is given in Figure 4.9 below. Due to concomitant field effects, diffusion weighting applied along the z-axis gave a significant attenuation gradient along the phase encoding direction y in the acquired slice at a 40 mm offset from the isocenter. The uncompensated CG fields in the CODE- M_0 images cause an underestimation of ADC values in the anterior compared to overestimation of values in the posterior regions. This effect is not visible in the images obtained with either of the concomitant compensated waveforms. The distribution of values around the mean and median confirms the visual assessment. Whereas the MONO and COCO- M_0 results show similar values in all ROIs and the full cerebrum, the ADC values of the CODE- M_0 acquisition vary more strongly from region to region. Mean diffusivity (MD) values of the CODE- M_0 show a larger RMS deviation from the gold standard MONO acquisition compared to the CG-compensated COCO- M_0 results.

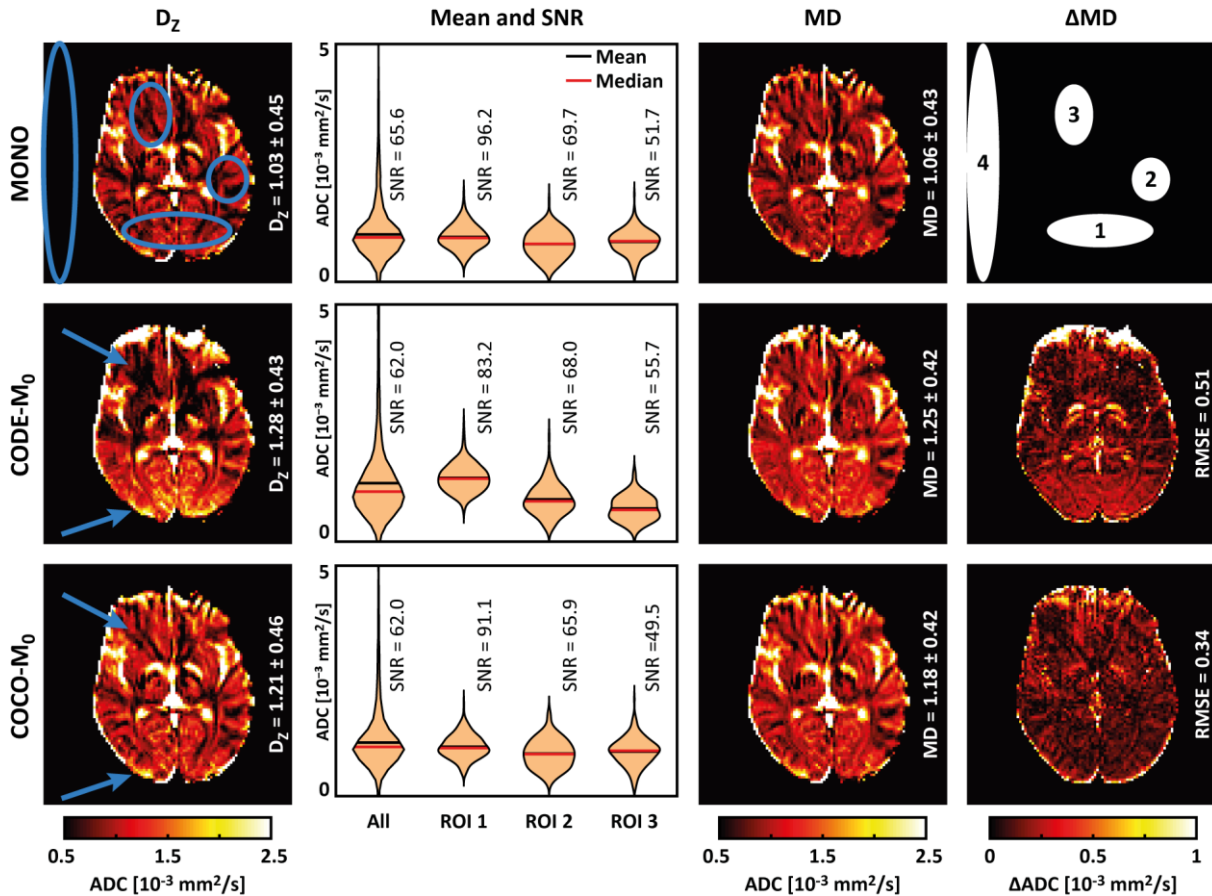


Figure 4.9: *In vivo* brain ADC maps, statistical analysis, and absolute deviation of MD values from the results obtained using MONO waveforms. Notice the spatially-varying attenuation along the phase encoding direction in the D_Z maps, and the overall error reduction in MD given by the RMSE for the CODE- M_0 vs. COCO- M_0 results. The diffusion-weighting was obtained using ultra-high maximum gradient amplitudes of $G_{max} = 270 \text{ mT/m}$, with other DEG waveform parameters being: $b = 400 \text{ s/mm}^2$, $S_{max} = 50 \text{ T/m/s}$ and $t_{EPI} = 16 \text{ ms}$.

The analysis was repeated for the data acquired at lower gradient strengths and higher b -values. Figure 4.10 shows the resulting ADC maps and distribution plots for each ROI. The ADC values are more uniformly distributed between different regions, indicating less spatial variation. However, the effect is less significant than at higher gradient amplitudes.

There is a global signal offset in the ADC values obtained with COCO- M_0 waveforms, resulting in a large RMSE despite having more uniform mean values throughout the inspected ROIs. This is also evident in the lower SNR obtained using COCO- M_0 waveforms. The SNR was calculated on the raw magnitude images, where a lower value is indicative of signal attenuation causing an overestimation of values in the final ADC maps. A similar global offset was observed in other brain scans performed. Possible explanations might include unaccounted gradient non-linearities, gradient amplifier limitations, or imperfect refocusing due to timing discrepancies in the actual vs. designed waveforms. The causes remain to be investigated in future work.

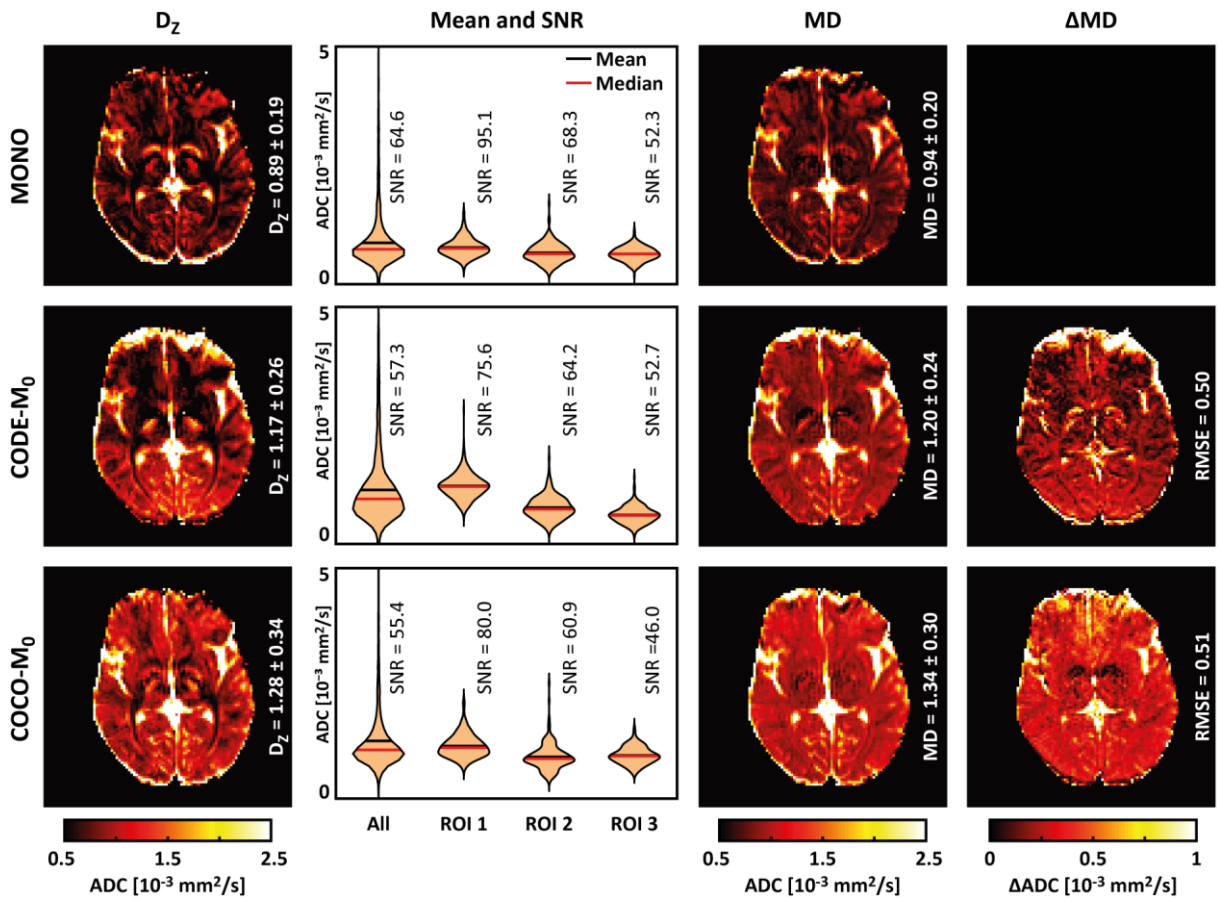


Figure 4.10: *In vivo* brain ADC maps acquired at $G_{max} = 150 \text{ mT/m}$ and $b = 500 \text{ s/mm}^2$. The images were obtained of an axial slice passing at a distance $d_z = 40 \text{ mm}$ parallel to the slice containing the magnetic isocenter. The previously observed attenuation gradient along the y -axis in the CODE results is still present, but less significant at the lower gradient amplitudes.

4.2.3 In Vivo Cardiac DTI

The cardiac imaging protocol described in section 3.2.3 was utilized to acquire data *in vivo*. From the acquired data, diffusion tensors were reconstructed, and the helix angle (HA) was calculated in short axis cross-sections through the myocardium. The results of the analysis are visualized in Figure 4.11, with the HA displayed for each voxel evaluated using data from each of the investigated methods: MOCO, COCO- M_2 and CODE- M_2 .

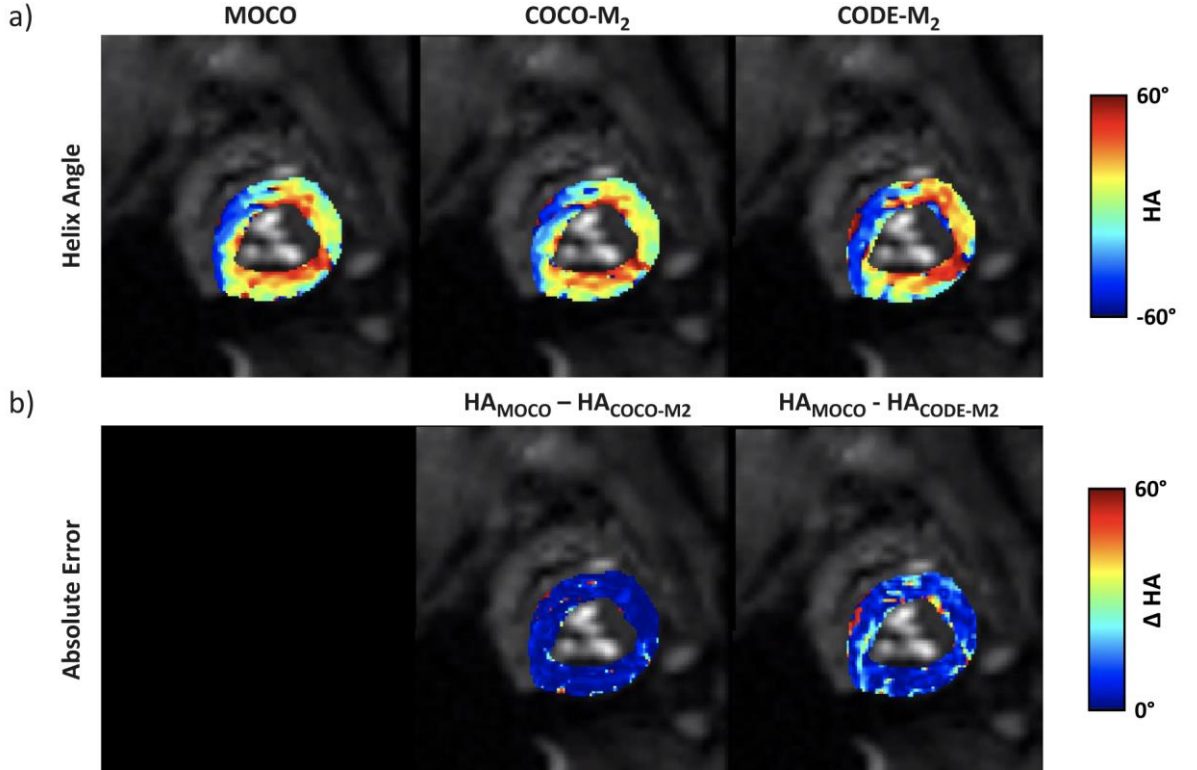


Figure 4.11: Visualization of *in vivo* heart helix angle and absolute errors. The obtained HA values of each voxel (a) are subtracted from the MOCO gold standard values to obtain the absolute errors (b). The images were obtained using waveforms designed using the following constraints: $b = 500 \text{ s/mm}^2$, $G_{max} = 150 \text{ mT/m}$, $S_{max} = 50 \text{ T/m/s}$, $t_{EPI} = 16 \text{ ms}$.

The obtained slice is slightly skewed, resulting in underestimated HA values in the left side and overestimated in the right side of the myocardium on the images. Using the results of the symmetric state-of-the-art waveforms as the gold standard, the absolute deviation was evaluated for the results obtained from the asymmetric waveforms. The CODE- M_2 waveforms show larger remaining absolute errors, particularly in the outer edges of the tissue, at the contours of the endo- and epicardium. The HA from the COCO- M_2 waveforms largely match the gold standard in all but a few voxels. The echo time was the same for all methods and a more detailed comparison of the methods would necessarily include reducing echo time to the minimal value permitted by each waveform in question. Cardiac diffusion MRI is particularly susceptible to motion artifacts.

5 Conclusion

In the presented work a convex optimization framework was realized and used to design asymmetric DEG waveforms that compensate effects of concomitant gradient fields in the full imaging volume and up to second order bulk motion effects. These show notable similarity to recently published ODGD waveforms (61), but were obtained in considerably shorter optimization times. The asymmetric design allows an increased encoding efficiency, a reduction in TE, and an increase in SNR compared to traditional symmetric DEG designs. The concomitant compensated (COCO) waveforms display a reduced impact of concomitant field effects inducing spatially-dependent signal bias compared to asymmetric waveforms without compensation (CODE). This is shown through ADC analysis and increased homogeneity in phantom and *in vivo* brain experiments. At the investigated gradient amplitudes up to $G_{max} = 270 \text{ mT/m}$, these perturbations become increasingly significant and compensation indispensable, particularly in areas farther away from the isocenter. This is highly relevant for three-dimensional imaging with large FOV. The penalty in increased encoding time compared to CODE waveforms was modest and brought along additional benefits in bulk motion robustness due to lower maximum values and variance in gradient moment and concomitant field residual phase evolution throughout the encoding. Overall, the asymmetric design allows a longer EPI readout enabling high-resolution diffusion MRI applications at high gradient field strengths.

The investigated approach was limited by a need for offline optimization. An implementation on the MR system allowing selection and on-the-fly waveform optimization for desired parameters is essential for clinical adoption. More importantly, eddy-current effects were not corrected in the optimized waveforms, which impacted diffusion encoding quality and caused ghosting artifacts. This problem has been addressed with similar optimization approaches, whereby eddy currents of a single time constant have been effectively nulled (58,60). A more comprehensive approach could expand the optimization with constraints defined on prospective field measurements, such as through a GIRF (94) approach as investigated in early stages of this work, or employ concurrent field monitoring (81,82,95) to comprehensively characterize and correct gradient effects.

Gradient optimization is potentially valuable for diffusion imaging and is receiving increasing attention (3,58–61,96). The parameter space for diffusion is not well explored and potential improvements can be made through unconventional pulse sequence design. Other approaches to explore the full MR acquisition parameter space, such as the recently introduced AUTOSEQ (97), could prove to be fruitful for improving clinical value of diffusion imaging as well as potentially creating entirely new applications and contrast mechanisms with atypical pulse sequence designs. The potential benefits of ultra-high gradient field strengths are also largely unexplored.

Appendix

The code used for gradient waveform optimization, along with appropriate examples, is available under the following link:

https://github.com/alen-mujkanovic/convex_diffusion

Bibliography

1. Le Bihan D, Poupon C, Amadon A, Lethimonnier F. Artifacts and pitfalls in diffusion MRI. *J. Magn. Reson. Imaging* 2006;24:478–488. doi: 10.1002/jmri.20683.
2. Baron CA, Lebel RM, Wilman AH, Beaulieu C. The effect of concomitant gradient fields on diffusion tensor imaging. *Magn. Reson. Med.* 2012;68:1190–1201. doi: 10.1002/mrm.24120.
3. Aliotta E, Wu HH, Ennis DB. Convex optimized diffusion encoding (CODE) gradient waveforms for minimum echo time and bulk motion-compensated diffusion-weighted MRI. *Magn. Reson. Med.* 2017;77:717–729. doi: 10.1002/mrm.26166.
4. Carr HY, Purcell EM. Effects of Diffusion on Free Precession in Nuclear Magnetic Resonance Experiments. *Phys. Rev.* 1954;94:630–638. doi: 10.1103/PhysRev.94.630.
5. Stejskal EO, Tanner JE. Spin diffusion measurements: Spin echoes in the presence of a time-dependent field gradient. *J. Chem. Phys.* 1965;42:288–292. doi: 10.1063/1.1695690.
6. Lauterbur PC. Image formation by induced local interactions. Examples employing nuclear magnetic resonance. *Nat. (London, United Kingdom)* 1973;242:190–191. doi: 10.1038/242190a0.
7. Le Bihan, D.; Breton E. Imagerie de diffusion *in vivo* par résonance magnétique nucléaire. *Comptes-Rendus l'Academie des Sci.* 1985;93:27–34.
8. Le Bihan D, Breton E, Lallemand D, Grenier P, Cabanis E, Laval-Jeantet M. MR imaging of intravoxel incoherent motions: application to diffusion and perfusion in neurologic disorders. *Radiology* 1986;161:401–407. doi: 10.1148/radiology.161.2.3763909.
9. Mansfield P. Multi-planar image formation using NMR spin echoes. *J. Phys. Chem.* 1977;10:55–58.
10. Stehling M, Turner R, Mansfield P. Echo-planar imaging: magnetic resonance imaging in a fraction of a second. *Science (80-.).* 1991;254:43–50. doi: 10.1126/science.1925560.
11. Turner R, Le Bihan D, Maier J, Vavrek R, Hedges LK, Pekar J. Echo-planar imaging of intravoxel incoherent motion. *Radiology* 1990;177:407–414. doi: 10.1148/radiology.177.2.2217777.
12. Basser PJ, Mattiello J, LeBihan D. MR diffusion tensor spectroscopy and imaging. *Biophys. J.* 1994;66:259–267. doi: 10.1016/S0006-3495(94)80775-1.
13. Hasan KM, Parker DL, Alexander AL. Comparison of gradient encoding schemes for diffusion-tensor MRI. *J. Magn. Reson. Imaging* 2001;13:769–780. doi: 10.1002/jmri.1107.
14. Le Bihan D. The “wet mind”: Water and functional neuroimaging. *Phys. Med. Biol.* 2007;52. doi: 10.1088/0031-9155/52/7/R02.

15. Iima M, Le Bihan D. Clinical Intravoxel Incoherent Motion and Diffusion MR Imaging: Past, Present, and Future. *Radiology* 2016;278:13–32. doi: 10.1148/radiol.2015150244.
16. Dyvorne HA, Galea N, Nevers T, et al. Diffusion-weighted Imaging of the Liver with Multiple b Values: Effect of Diffusion Gradient Polarity and Breathing Acquisition on Image Quality and Intravoxel Incoherent Motion Parameters—A Pilot Study. *Radiology* 2013;266:920–929. doi: 10.1148/radiol.12120686.
17. Dong Q, Welsh RC, Chenevert TL, Carlos RC, Maly-Sundgren P, Gomez-Hassan DM, Mukherji SK. Clinical applications of diffusion tensor imaging. *J. Magn. Reson. Imaging* 2004;19:6–18. doi: 10.1016/j.wneu.2013.07.083.
18. Nguyen C, Fan Z, Xie Y, Dawkins J, Tseliou E, Bi X, Sharif B, Dharmakumar R, Marbán E, Li D. In vivo contrast free chronic myocardial infarction characterization using diffusion-weighted cardiovascular magnetic resonance. *J. Cardiovasc. Magn. Reson.* 2014;16:1–10. doi: 10.1186/s12968-014-0068-y.
19. Nguyen C, Lu M, Fan Z, Bi X, Kellman P, Zhao S, Li D. Contrast-free detection of myocardial fibrosis in hypertrophic cardiomyopathy patients with diffusion-weighted cardiovascular magnetic resonance. *J. Cardiovasc. Magn. Reson.* 2015;17:1–7. doi: 10.1186/s12968-015-0214-1.
20. Tae WS, Ham BJ, Pyun SB, Kang SH, Kim BJ. Current clinical applications of diffusion-tensor imaging in neurological disorders. *J. Clin. Neurol.* 2018;14:129–140. doi: 10.3988/jcn.2018.14.2.129.
21. Baliyan V, Das CJ, Sharma R, Gupta AK. Diffusion weighted imaging: Technique and applications. *World J. Radiol.* 2016;8:785. doi: 10.4329/wjr.v8.i9.785.
22. McNab JA, Edlow BL, Witzel T, et al. The Human Connectome Project and beyond: Initial applications of 300mT/m gradients. *Neuroimage* 2013;80:234–245. doi: 10.1016/j.neuroimage.2013.05.074.
23. Setsompop K, Kimmlingen R, Eberlein E, et al. Pushing the limits of in vivo diffusion MRI for the Human Connectome Project. *Neuroimage* 2013;80:220–233. doi: 10.1016/j.neuroimage.2013.05.078.
24. Yendiki A. Automated probabilistic reconstruction of white-matter pathways in health and disease using an atlas of the underlying anatomy. *Front. Neuroinform.* 2011;5:1–12. doi: 10.3389/fninf.2011.00023.
25. Sosnovik DE, Wang R, Dai G, Reese TG, Wedeen VJ. Diffusion MR tractography of the heart. *J. Cardiovasc. Magn. Reson.* 2009;11:1–15. doi: 10.1186/1532-429X-11-47.
26. Mekkaoui C, Porayette P, Jackowski MP, Kostis WJ, Dai G, Sanders S, Sosnovik DE. Diffusion MRI Tractography of the Developing Human Fetal Heart. *PLoS One* 2013;8:4–9. doi: 10.1371/journal.pone.0072795.
27. Mekkaoui C, Jackowski MP, Kostis WJ, Stoeck CT, Thiagalingam A, Reese TG, Reddy VY, Ruskin JN, Kozerke S, Sosnovik DE. Myocardial scar delineation using diffusion tensor magnetic resonance tractography. *J. Am. Heart Assoc.* 2018;7:1–10. doi: 10.1161/JAHA.117.007834.
28. Hahn EL. Spin Echoes. *Phys. Rev.* 1950;80:580–594. doi: 10.1103/PhysRev.80.580.
29. Kingsley PB, Monahan WG. Selection of the Optimum b Factor for Diffusion-Weighted Magnetic Resonance Imaging Assessment of Ischemic Stroke. *Magn. Reson. Med.* 2004;51:996–1001. doi: 10.1002/mrm.20059.

30. Trouard TP, Sabharwal Y, Altbach MI, Gmitro AF. Analysis and comparison of motion-correction techniques in Diffusion-Weighted Imaging. *J. Magn. Reson. Imaging* 1996;6:925–935. doi: 10.1002/jmri.1880060614.
31. Stoeck CT, Von Deuster C, GeneT M, Atkinson D, Kozerke S. Second-order motion-compensated spin echo diffusion tensor imaging of the human heart. *Magn. Reson. Med.* 2016;75:1669–1676. doi: 10.1002/mrm.25784.
32. Gamper U, Boesiger P, Kozerke S. Diffusion imaging of the in vivo heart using spin echoes—considerations on bulk motion sensitivity. *Magn. Reson. Med.* 2007;57:331–337. doi: 10.1002/mrm.21127.
33. Ozaki M, Inoue Y, Miyati T, Hata H, Mizukami S, Komi S, Matsunaga K, Woodhams R. Motion artifact reduction of diffusion-weighted MRI of the liver: Use of velocity-compensated diffusion gradients combined with tetrahedral gradients. *J. Magn. Reson. Imaging* 2013;37:172–178. doi: 10.1002/jmri.23796.
34. Pruessmann KP, Weiger M, Scheidegger MB, Boesiger P. SENSE: sensitivity encoding for fast MRI. *Magn. Reson. Med.* 1999;42:952–62. doi: 10.1002/(SICI)1522-2594(199911)42:5<952::AID-MRM16>3.0.CO;2-S.
35. Griswold MA, Jakob PM, Heidemann RM, Nittka M, Jellus V, Wang J, Kiefer B, Haase A. Generalized Autocalibrating Partially Parallel Acquisitions (GRAPPA). *Magn. Reson. Med.* 2002;47:1202–1210. doi: 10.1002/mrm.10171.
36. Buehrer M, Curcic J, Boesiger P, Kozerke S. Prospective self-gating for simultaneous compensation of cardiac and respiratory motion. *Magn. Reson. Med.* 2008;60:683–690. doi: 10.1002/mrm.21697.
37. Wundrak S, Paul J, Ulrici J, Hell E, Geibel MA, Bernhardt P, Rottbauer W, Rasche V. A self-gating method for time-resolved imaging of nonuniform motion. *Magn. Reson. Med.* 2016;76:919–925. doi: 10.1002/mrm.26000.
38. Uribe S, Beerbaum P, Sørensen TS, Rasmussen A, Razavi R, Schaeffter T. Four-dimensional (4D) flow of the whole heart and great vessels using real-time respiratory self-gating. *Magn. Reson. Med.* 2009;62:984–992. doi: 10.1002/mrm.22090.
39. Reese TG, Weisskoff RM, Smith RN, Rosen BR, Dinsmore RE, Wedeen VJ. Imaging myocardial fiber architecture in vivo with magnetic resonance. *Magn. Reson. Med.* 1995;34:786–791. doi: 10.1002/mrm.1910340603.
40. Wiegell MR, Larsson HBW, Wedeen VJ. Fiber Crossing in Human Brain Depicted with Diffusion Tensor MR Imaging. *Radiology* 2000;217:897–903. doi: 10.1148/radiology.217.3.r00nv43897.
41. Bucci M, Mandelli ML, Berman JI, Amirbekian B, Nguyen C, Berger MS, Henry RG. Quantifying diffusion MRI tractography of the corticospinal tract in brain tumors with deterministic and probabilistic methods. *NeuroImage Clin.* 2013;3:361–368. doi: 10.1016/j.nicl.2013.08.008.
42. O'Donnell LJ, Westin CF. An introduction to diffusion tensor image analysis. *Neurosurg. Clin. N. Am.* 2011;22:185–196. doi: 10.1016/j.nec.2010.12.004.
43. Schilling K, Gao Y, Janve V, Stepniewska I, Landman BA, Anderson AW. Can increased spatial resolution solve the crossing fiber problem for diffusion MRI? *NMR Biomed.* 2017;30:1–16. doi: 10.1002/nbm.3787.
44. Scott AD, Ferreira P, Nielles-Valdespin S, McGill L-A, Pennell DJ, Firmin D. Directions vs. averages: an in-vivo comparison for cardiac DTI. *J. Cardiovasc. Magn. Reson.* 2015;17:P25. doi: 10.1186/1532-429X-17-S1-P25.

45. Teh I, McClymont D, Burton RAB, Maguire ML, Whittington HJ, Lygate CA, Kohl P, Schneider JE. Resolving Fine Cardiac Structures in Rats with High-Resolution Diffusion Tensor Imaging. *Sci. Rep.* 2016;6:30573. doi: 10.1038/srep30573.
46. Minati L, Węglarz WP. Physical foundations, models, and methods of diffusion magnetic resonance imaging of the brain: A review. *Concepts Magn. Reson. Part A* 2007;30A:278–307. doi: 10.1002/cmr.a.20094.
47. Yendíki A. Diffusion MRI : Where to go from here. 2018:Conference talk, 3.5.2018, Brainhack Boston.
48. Jezzard P, Barnett AS, Pierpaoli C. Characterization of and correction for eddy current artifacts in echo planar diffusion imaging. *Magn. Reson. Med.* 1998;39:801–812. doi: 10.1002/mrm.1910390518.
49. Norris DG, Hutchison JM. Concomitant magnetic field gradients and their effects on imaging at low magnetic field strengths. *Magn. Reson. Imaging* 1990;8:33–7. doi: 10.1016/0730-725X(90)90209-K.
50. Nagy Z, Weiskopf N, Alexander DC, Deichmann R. A method for improving the performance of gradient systems for diffusion-weighted MRI. *Magn. Reson. Med.* 2007;58:763–768. doi: 10.1002/mrm.21379.
51. Simonetti OP, Duerk JL, Chankong V. An optimal design method for magnetic resonance imaging gradient waveforms. *IEEE Trans. Med. Imaging* 1993;12:350–360. doi: 10.1109/42.232266.
52. Simonetti OP, Duerk JL, Chankong V. MRI gradient waveform design by numerical optimization. *Magn. Reson. Med.* 1993;29:498–504. doi: 10.1002/mrm.1910290411.
53. Hargreaves BA, Nishimura DG, Conolly SM. Time-Optimal Multidimensional Gradient Waveform Design for Rapid Imaging. *Magn. Reson. Med.* 2004;51:81–92. doi: 10.1002/mrm.10666.
54. Derbyshire JA, Herzka DA, McVeigh ER, Lederman RJ. Efficient implementation of hardware-optimized gradient sequences for real-time imaging. *Magn. Reson. Med.* 2010;64:1814–1820. doi: 10.1002/mrm.22211.
55. Loecher M, Ennis DB. Velocity reconstruction with nonconvex optimization for low-velocity-encoding phase-contrast MRI. *Magn. Reson. Med.* 2018;80:42–52. doi: 10.1002/mrm.26997.
56. Drobniak I, Alexander DC. Optimising time-varying gradient orientation for microstructure sensitivity in diffusion-weighted MR. *J. Magn. Reson.* 2011;212:344–354. doi: 10.1016/j.jmr.2011.07.017.
57. Middione MJ, Wu HH, Ennis DB. Convex gradient optimization for increased spatiotemporal resolution and improved accuracy in phase contrast MRI. *Magn. Reson. Med.* 2014;72:1552–1564. doi: 10.1002/mrm.25059.
58. Yang G, Mcnab JA. Eddy current nulled constrained optimization of isotropic diffusion encoding gradient waveforms. *Magn. Reson. Med.* 2018. doi: 10.1002/mrm.27539.
59. Sjölund J, Szczepankiewicz F, Nilsson M, Topgaard D, Westin C-F, Knutsson H. Constrained optimization of gradient waveforms for generalized diffusion encoding. *J. Magn. Reson.* 2015;261:157–168. doi: 10.1016/J.JMR.2015.10.012.

60. Aliotta E, Moulin K, Ennis DB. Eddy current–nulled convex optimized diffusion encoding (EN-CODE) for distortion-free diffusion tensor imaging with short echo times. *Magn. Reson. Med.* 2018;79:663–672. doi: 10.1002/mrm.26709.
61. Peña-Nogales Ó, Zhang Y, Wang X, de Luis-Garcia R, Aja-Fernández S, Holmes JH, Hernando D. Optimized Diffusion-Weighting Gradient Waveform Design (ODGD) formulation for motion compensation and concomitant gradient nulling. *Magn. Reson. Med.* 2018;1–15. doi: 10.1002/mrm.27462.
62. Andersen CH. Time-Dependent Statistical Mechanics. In: Advanced Physical Chemistry. Palo Alto, California: Stanford University; 2009. pp. 135–159.
63. Mori S, Tournier DJ. Introduction to Diffusion Tensor Imaging. Second edi. Academic Press - Elsevier; 2014. doi: 10.1016/C2011-0-07607-X.
64. Bloch F. Nuclear induction. *Phys. Rev.* 1946;70:460–474. doi: 10.1103/PhysRev.70.460.
65. Torrey HC. Bloch equations with diffusion terms. *Phys. Rev.* 1956;104:563–565. doi: 10.1103/PhysRev.104.563.
66. Kozerke S. Magnetic Resonance Imaging in Medicine. 2016:Lecture notes ETH Zürich 227-0948-00L.
67. Le Bihan D. Apparent Diffusion Coefficient and Beyond: What Diffusion MR Imaging Can Tell Us about Tissue Structure. *Radiology* 2013;268:318–322. doi: 10.1148/radiol.13130420.
68. Holz M, Heil SR, Sacco A. Temperature-dependent self-diffusion coefficients of water and six selected molecular liquids for calibration in accurate ¹H NMR PFG measurements. *Phys. Chem. Chem. Phys.* 2000;2:4740–4742. doi: 10.1039/b005319h.
69. Kolff-Gart AS, Pouwels PJW, Noij DP, Ljumanovic R, Vandecaveye V, De Keyzer F, De Bree R, De Graaf P, Knol DL, Castelijns JA. Diffusion-weighted imaging of the head and neck in healthy subjects: Reproducibility of ADC values in different MRI systems and repeat sessions. *Am. J. Neuroradiol.* 2015;36:384–390. doi: 10.3174/ajnr.A4114.
70. Nguyen C, Fan Z, Xie Y, Pang J, Speier P, Bi X, Kobashigawa J, Li D. In vivo diffusion-tensor MRI of the human heart on a 3 tesla clinical scanner: An optimized second order (M2) motion compensated diffusion-preparation approach. *Magn. Reson. Med.* 2016;76:1354–1363. doi: 10.1002/mrm.26380.
71. Mattiello J, Basser PJ, Le Bihan D. The b matrix in diffusion tensor echo-planar imaging. *Magn. Reson. Med.* 1997;37:292–300. doi: 10.1002/mrm.1910370226.
72. Jellison BJ, Field AS, Medow J, Lazar M, Salamat MS, Alexander AL. Diffusion tensor imaging of cerebral white matter: a pictorial review of physics, fiber tract anatomy, and tumor imaging patterns. *AJNR. Am. J. Neuroradiol.* 2004;25:356–69.
73. Nguyen C, Fan Z, Sharif B, He Y, Dharmakumar R, Berman DS, Li D. In vivo three-dimensional high resolution cardiac diffusion-weighted MRI: A motion compensated diffusion-prepared balanced steady-state free precession approach. *Magn. Reson. Med.* 2014;72:1257–1267. doi: 10.1002/mrm.25038.
74. Lyseggen E, Rabben SI, Skulstad H, Urheim S, Risoe C, Smiseth OA. Myocardial acceleration during isovolumic contraction: Relationship to contractility. *Circulation* 2005;111:1362–1369. doi: 10.1161/01.CIR.0000158432.86860.A6.

75. Shibukawa S, Miyati T, Ohno N, Niwa T, Imai Y, Ogino T, Muro I. Acceleration motion compensation DWI for measuring intraventricular temperature. ISMRM 24th Annu. Meet. Exhib. 2016:Poster Submision 3029, Diffusion 1 Exhibition.
76. Welsh CL, Di Bella EVR, Hsu EW. Higher-Order Motion-Compensation for in Vivo Cardiac Diffusion Tensor Imaging in Rats. *IEEE Trans. Med. Imaging* 2015;34:1843–1853. doi: 10.1109/TMI.2015.2411571.
77. Boesch C, Gruetter R, Martin E. Temporal and spatial analysis of fields generated by eddy currents in superconducting magnets: optimization of corrections and quantitative characterization of magnet/gradient systems. *Magn. Reson. Med.* 1991;20:268–84. doi: 10.1002/mrm.1910200209.
78. Jehenson P, Westphal M, Schuff N. Analytical method for the compensation of eddy-current effects induced by pulsed magnetic field gradients in NMR systems. *J. Magn. Reson.* 1990;90:264–278. doi: 10.1016/0022-2364(90)90133-T.
79. Van Vaals JJ, Bergman AH. Optimization of Eddy-Current Compensation. *J. Magn. Reson.* 1990;90:52–70.
80. Vannesjo SJ, Dietrich BE, Pavan M, Brunner DO, Wilm BJ, Barmet C, Pruessmann KP. Field camera measurements of gradient and shim impulse responses using frequency sweeps. *Magn. Reson. Med.* 2014;72:570–583. doi: 10.1002/mrm.24934.
81. Chan RW, Von Deuster C, Giese D, Stoeck CT, Harmer J, Aitken AP, Atkinson D, Kozerke S. Characterization and correction of eddy-current artifacts in unipolar and bipolar diffusion sequences using magnetic field monitoring. *J. Magn. Reson.* 2014;244:74–84. doi: 10.1016/j.jmr.2014.04.018.
82. Wilm BJ, Nagy Z, Barmet C, et al. Diffusion MRI with concurrent magnetic field monitoring. *Magn. Reson. Med.* 2015;74:925–933. doi: 10.1002/mrm.25827.
83. Wilm BJ. Diffusion-Weighted MRI – Volume Selection, Field Monitoring and Image Reconstruction. ETH Zürich; 2009. doi: 10.3929/ethz-a-005820836.
84. Bernstein MA, King KE, Zhou XJ, Fong W. Handbook of MRI Pulse Sequences. Elsevier Inc.; 2004.
85. Zhou XJ, Tan SG, Bernstein MA. Artifacts induced by concomitant magnetic field in fast spin-echo imaging. *Magn. Reson. Med.* 1998;40:582–591. doi: 10.1002/mrm.1910400411.
86. Meier C, Zwanger M, Feiweier T, Porter D. Concomitant field terms for asymmetric gradient coils: Consequences for diffusion, flow, and echo-planar imaging. *Magn. Reson. Med.* 2008;60:128–134. doi: 10.1002/mrm.21615.
87. Szczepankiewicz F, Nilsson M. Maxwell-compensated waveform design for asymmetric diffusion encoding. ISMRM Abstr. Submiss. 2018:6–9.
88. Boyd S, Vandenberghe L. Convex Optimization. Seventh Ed. Cambridge: Cambridge University Press; 2004. doi: 10.1016/B978-012428751-8/50019-7.
89. Lofberg J. YALMIP : a toolbox for modeling and optimization in MATLAB. In: 2004 IEEE International Symposium on Computer Aided Control Systems Design. IEEE; 2004. pp. 284–289. doi: 10.1109/CACSD.2004.1393890.
90. Keil B, Blau JN, Biber S, Hoecht P, Tountcheva V, Setsompop K, Triantafyllou C, Wald LL. A 64-channel 3T array coil for accelerated brain MRI. *Magn. Reson. Med.* 2013;70:248–258. doi: 10.1002/mrm.24427.

91. Nguyen CT, Dawkins J, Bi X, Marbán E, Li D. Diffusion Tensor Cardiac Magnetic Resonance Reveals Exosomes From Cardiosphere-Derived Cells Preserve Myocardial Fiber Architecture After Myocardial Infarction. *JACC Basic to Transl. Sci.* 2018;3:97–109. doi: 10.1016/j.jacbts.2017.09.005.
92. Schieban K, Mekkaoui C, Sosnovik DE, Kozerke S. Characterization of high performance gradient system for spin echo cardiac DTI. ETH Zürich; 2014.
93. Griffanti L, Baglio F, Preti MG, Cecconi P, Rovaris M, Baselli G, Laganà MM. Signal-to-noise ratio of diffusion weighted magnetic resonance imaging: Estimation methods and in vivo application to spinal cord. *Biomed. Signal Process. Control* 2012;7:285–294. doi: 10.1016/j.bspc.2011.06.003.
94. Vannesjo SJ, Haeberlin M, Kasper L, Pavan M, Wilm BJ, Barmet C, Pruessmann KP. Gradient system characterization by impulse response measurements with a dynamic field camera. *Magn. Reson. Med.* 2013;69:583–593. doi: 10.1002/mrm.24263.
95. Barmet C, De Zanche N, Pruessmann KP. Spatiotemporal magnetic field monitoring for MR. *Magn. Reson. Med.* 2008;60:187–197. doi: 10.1002/mrm.21603.
96. Majeed W, Kalra P, Kolipaka A. Motion Compensated, Optimized Diffusion Encoding (MODE) Gradient Waveforms. In: ISMRM Abstract Submission. Paris: ISMRM; 2018. p. Submission 1614.
97. Zhu B, Liu JZ, Koonjoo N, Rosen BR, Rosen MS. AUTOmated pulse SEQuence generation (AUTOSEQ) using Bayesian reinforcement learning in an MRI physics simulation environment. In: ISMRM. ; 2018.

Declaration of originality

The signed declaration of originality is a component of every semester paper, Bachelor's thesis, Master's thesis and any other degree paper undertaken during the course of studies, including the respective electronic versions.

Lecturers may also require a declaration of originality for other written papers compiled for their courses.

I hereby confirm that I am the sole author of the written work here enclosed and that I have compiled it in my own words. Parts excepted are corrections of form and content by the supervisor.

Title of work (in block letters):

Asymmetric Diffusion Encoding for High-Resolution Diffusion Tensor Imaging

Authored by (in block letters):

For papers written by groups the names of all authors are required.

Name(s):

Mujkanović

First name(s):

Alen

With my signature I confirm that

- I have committed none of the forms of plagiarism described in the '[Citation etiquette](#)' information sheet.
- I have documented all methods, data and processes truthfully.
- I have not manipulated any data.
- I have mentioned all persons who were significant facilitators of the work.

I am aware that the work may be screened electronically for plagiarism.

Place, date

Signature(s)

For papers written by groups the names of all authors are required. Their signatures collectively guarantee the entire content of the written paper.